# Support information

## Spin-Regulated *d-p* Hybridization Enables High-Energy-Density and Wide-Temperature Operation of $Na_3V_2(PO_4)_2O_2F$-Type Cathodes for Sodium-Ion Batteries

*Qiang Fu,[a] Qin He,[a] Fangxiang Song,[a] Xianquan Ao,*[a,b] Hanxiao Liu,[c] Yang Cao,[a,b] Rong Li,*[a] Keliang Wang,[d] Jing Li,[d] Cuiqin Li,[a] and Yao Xiao*[c]*

[a] School of Chemistry and Chemical Engineering, Guizhou University, Guiyang 550025, P. R. China. E-mail: aoxianquan@163.com (Xianquan Ao), Li@gzu.edu.cn (Rong Li)

[b] Guizhou Provincial Key Laboratory of Green Catalysis and Materials for resource conversion, Guiyang 550025, P. R China

[c] College of Chemistry and Materials Engineering, Wenzhou University, Wenzhou, 325035, P. R. China. E-mail: xiaoyao@wzu.edu.cn (Yao Xiao)

[d] School of Brewing Engineering, Moutai Institute, Renhuai 564501 P. R. China

**Keywords**: $Na_3V_2(PO_4)_2O_2F$, d–p Orbital Hybridization, High rate, Multifunctional battery, sodium ion battery

## 1. Materials Synthesis

**Preparation of samples with varying $Fe^{3+}/F^-$ doping levels.** Firstly, 0.03 mol NaF(Aladdin, ≥99.9%), 0.035 mol $HONH_2 \cdot HCl$(Aladdin, ≥99%), 0.02-x mol $NaVO_3$(Aladdin, ≥99%), and x mol $Fe(NO_3)_3 \cdot 9H_2O$(Aladdin，≥99.9%) (x=0.0005, 0.001, 0.0015 ) were dissolved in 40 mL deionized water to obtain solution A. Secondly, 0.035 mol $NaH_2PO_4$(Aladdin，≥99%) was dissolved in 10 mL deionized water to prepare solution B. Subsequently, once solution A developed a blue-green coloration, solution B was slowly added dropwise. Finally, the resulting mixture was transferred into a 100 mL Teflon-lined stainless-steel autoclave, heated at 150 °C for 10 h, and then allowed to cool naturally to room temperature. The precipitate obtained was washed three times with deionized water. After vacuum drying, the products obtained were $Na_3(VO)_2(PO_4)_2F$ (denoted as NVPOF), $Na_3(VO)_{1.95}Fe_{0.05}(PO_4)_2F_{1.05}$ (denoted as NVPOF-2.5%Fe), $Na_3(VO)_{1.9}Fe_{0.1}(PO_4)_2F_{1.1}$ (denoted as NVPOF-Fe), and $Na_3(VO)_{1.85}Fe_{0.15}(PO_4)_2F_{1.15}$ (denoted as NVPOF-7.5%Fe).

**Preparation of samples doped with different M elements (M = Sc, V, and Cr)**. The synthesis followed the procedure described above, wherein 1 mmol $Fe(NO_3)_3 \cdot 9H_2O$ was substituted, in separate batches, with 1 mmol $Sc_2(SO_4)_3 \cdot 8H_2O$ (MACKLIN，≥99.9%), 1.03 mmol vanadium acetylacetonate ($V(acac)_3$) (MACKLIN，≥97%), or 1 mmol $Cr(NO_3)_3 \cdot 9H_2O$(MACKLIN，≥99.9%). The resultant products were $Na_3(VO)_{1.9}Sc_{0.1}(PO_4)_2F_{1.1}$ (denoted as NVPOF-Sc), $Na_3(V^{4+}O)_{1.9}V^{3+}{}_{0.1}(PO_4)_2F_{1.1}$ (denoted as NVPOF-V), and $Na_3(VO)_{1.9}Cr_{0.1}(PO_4)_2F_{1.1}$ (denoted as NVPOF-Cr).

**Structure characterization.** The morphology of the samples was characterized using scanning electron microscopy (SEM, ZEISS Sigma 300) and transmission electron microscopy (TEM, JEOL JEM-F200). The crystal structure was analyzed by X-ray diffraction (XRD, Cu Kα radiation, Bruker D8 Advance), and the phase structure together with the doping level was refined via Rietveld analysis using the FullProf Suite software. [1] Schematic illustrations based on the refinement results were generated using VESTA software.[2] X-ray photoelectron spectroscopy (XPS, Thermo Scientific K-Alpha) was employed to examine the elemental states and orbital configurations of the samples and of electrode at different charge/discharge states. Following electrochemical cycling, the coin cells were disassembled, and the electrodes were rinsed with dimethyl carbonate prior to XPS characterization. Fourier transform

infrared spectroscopy (FT-IR, Bruker EQUINOX55) was performed to identify the vibrational modes of functional groups. Electron paramagnetic resonance (EPR) spectra of the prepared samples were recorded at room temperature using a Bruker EMXplus-6/1 spectrometer. In situ XRD (Bruker D8 Advance) measurements during electrochemical cycling were carried out using a custom-designed cell equipped with a beryllium window, operated over a voltage range of 2.0-4.3 V at 0.1 C (1 C = 130 mAh $g^{-1}$) for one complete cycle. Diffraction patterns were collected every 8 min. Ultraviolet–visible (UV-Vis) spectra were recorded using a PERSEE PTC-2 spectrophotometer to gain deeper insights into the optical properties of the materials. X-ray absorption near-edge structure (XANES) and extended X-ray absorption fine structure (EXAFS) spectra at the V K-edge were acquired at the Shanghai Synchrotron Radiation Facility (SSRF).

**Electrochemical testing**

**Half cell.** The cathode was fabricated by pressing a slurry containing active material (70 wt.%), conductive carbon black (20 wt.%), and polyvinylidene fluoride (10 wt. %) in N-methyl-2-pyrrolidone onto an aluminum foil and dried under vacuum at 100 °C for 10 h. The active-material mass loading was approximately 1.0-1.3 mg per electrode. Coin cells (CR2032) were assembled in an argon-filled glovebox. The electrolyte was 1 M $NaClO_4$in propylene carbonate (PC) with 2 vol% fluoroethylene carbonate (FEC) additive; sodium metal foil as anode, and a glass-fiber separator (Whatman, GF/D) was used. Electrochemical testing of all half cells was conducted on a battery testing system (LAND CT2001A, China) within a voltage window of 2.0–4.4 V. Galvanostatic intermittent titration technique (GITT) measurements were performed by applying a constant-current charge or discharge at 0.1 C for 10 min, followed by a 60 min relaxation to approach quasi-equilibrium. Cyclic voltammetry (CV) and electrochemical impedance spectroscopy (EIS) were carried out using an electrochemical workstation (CS Studio6, China).

**Full cell.** The cathode was fabricated by pressing a slurry containing Hard carbon active material (85 wt.%), conductive carbon black (10 wt.%), carboxymethyl cellulose polyvinylidene fluoride (2 wt. %), and styrene-butadiene rubber (3 wt.%) in an aqueous onto an aluminum foil and dried under vacuum at 100 °C for 10 h. The mass loading per electrode was approximately 0.6-0.8 mg. Half cells were assembled using sodium metal foil as the counter electrode and pre-sodiation by two cycles at a current density

of 50 mA $g^{-1}$; thereafter, NVPOF-Fe//HC full cells were assembled for performance evaluation. At ambient temperature, tests were conducted within a voltage window of 2.0-4.3 V, employing the same electrolyte as in the half cells. For 2C cycling at elevated temperature (45 °C), the electrolyte was the same as that used for the half cells, whereas 1C cycling at low temperature (-20 °C) employed 1 M $NaPF_6$ dissolved in diethylene glycol dimethyl ether (diglyme). The voltage window for the high/low temperature tests was 1.5-4.3 V.

**Computational Details.** To gain a comprehensive understanding of the electrochemical properties of the materials, first-principles calculations were performed using the Vienna ab initio Simulation Package (VASP). The projector-augmented wave (PAW) method was employed to describe the interactions between nuclei and electrons, and the exchange correlation potentials were treated within the generalized gradient approximation (GGA) using the Perdew-Burke-Ernzerhof (PBE) functional.[3-5] Spin polarization was switched on for all calculations, with a plane-wave cutoff energy of 520 eV. The convergence criterion for total energy was set to $1\times10^{-6}$eV, and that for atomic forces was set to 0.02 eV $Å^{-1}$. For the density of states (DOS) calculations, a 2 × 1 × 1 supercell was used together with a Monkhorst-Pack k-point mesh of 4 × 8 × 7. To account for the strong correlation among the 3d-orbital electrons of M (M = Sc, V, Cr, Fe), the GGA+U method was adopted, with U values of 3.3, 4.0, 3.1, 3.5, and 4.9 eV for $Sc^{3+}$, $V^{4+}$, $V^{3+}$, $Cr^{3+}$, and $Fe^{3+}$, respectively.[6-9] Chemical bonding analysis based on the crystal orbital Hamilton population (COHP) methodology was conducted using the LOBSTER package.[10] The diffusion pathways and associated energy barriers for $Na^+$ migration were calculated using the climbing-image nudged elastic band (CI-NEB) method.[11]

## 2. Supporting diagrams and tables

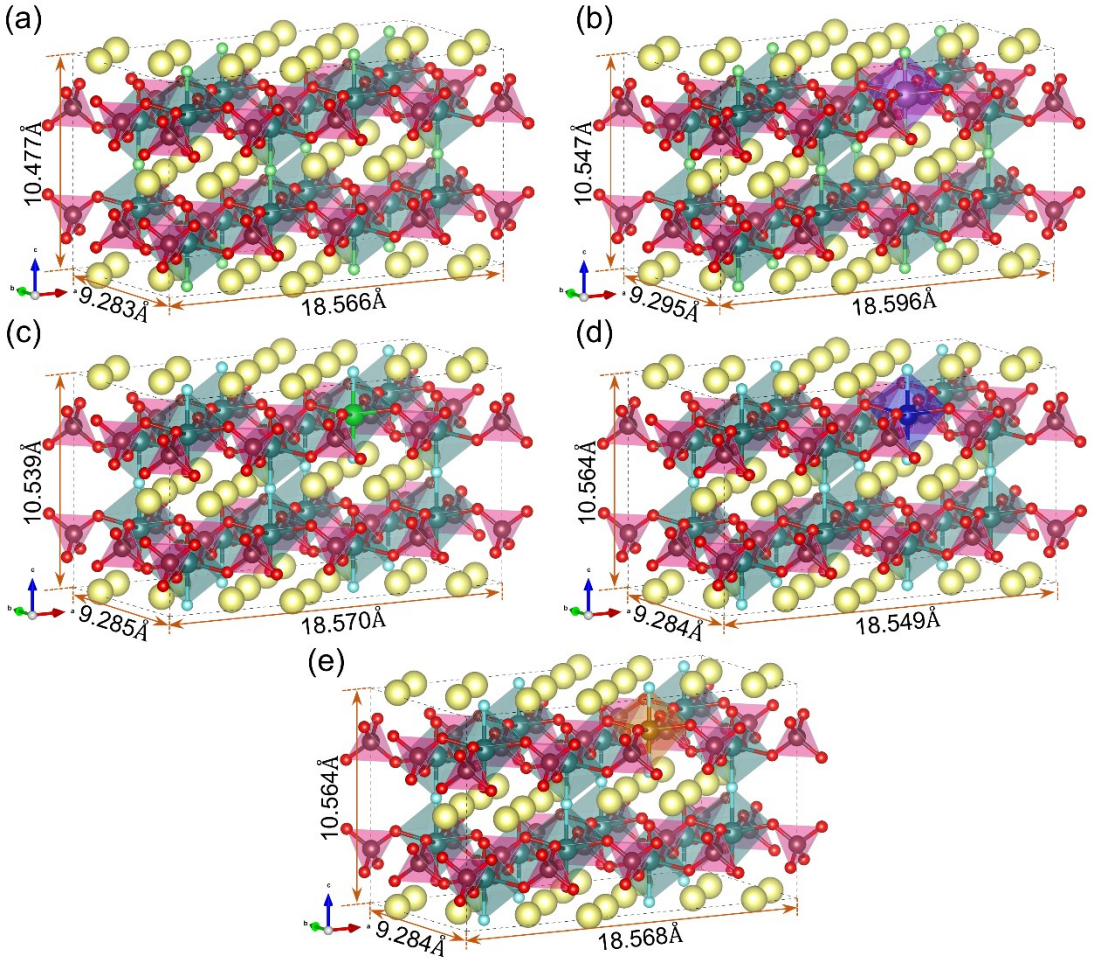


**Fig. S1.** Structural optimization results of (a) NVPOF, (b) NVPOF-Sc, (c) NVPOF-V, (d) NVPOF-Cr, and (e) NVPOF-Fe based on DFT calculations, the red, yellow, purple, green, blue, and orange spheres represent O, Na, Sc, V, Cr, and Fe elements, respectively.

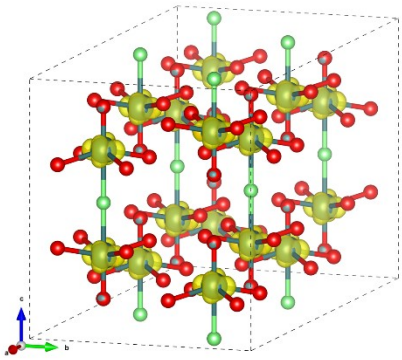

**Fig. S2.** NVPOF spin state.

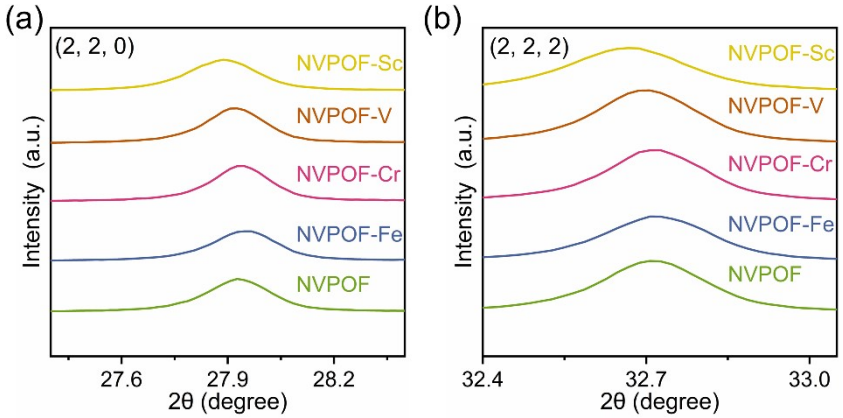


**Fig. S3.** Comparison of (a) (2,2,0) and (b) (2,2,2) characteristic peaks of NVPOF and NVPOF-M (M=Sc, V, Cr, and Fe).

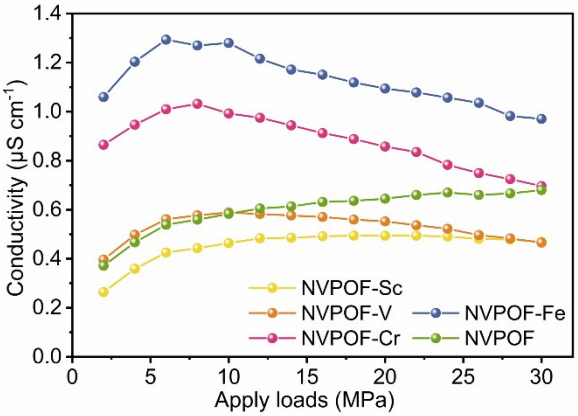


**Fig. S4.** The four-point probe conductivity results of NVPOF-M (M=Sc, V, Cr, Fe) and NVPOF under a load of 2–30MPa.

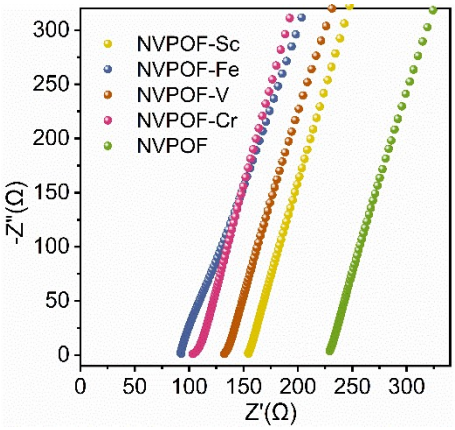


**Fig. S5.** Nyquist impedance plot at room temperature.

Note: A symmetric stainless-steel cell (SS|NVPOF-M|SS) was assembled to evaluate the ionic conductivity of NVPOF-M (M = Sc, V, Cr, and Fe) as well as pristine NVPOF. The nanopowders were pressed into pellets (10 mm in diameter; density = 1.3 g $cm^{-3}$). To mitigate poor solid–solid interfacial contact, 10 μL of electrolyte was added to the pellet prior to measurement. The ionic conductivity (σ) was calculated according to Eq. (1).

$$\sigma = L/(R \times S) \qquad \text{Eq. (1)}$$

Here, $L$ denotes the electrolyte thickness, $R$ the bulk resistance, and $S$ the interfacial contact area between the solid-state electrolyte (SSE) and the electrode. As indicated by the Eq. (1), when $L$ and $S$ are kept constant, the ionic conductivity (σ) is inversely proportional to $R$; a larger $R$ therefore corresponds to a smaller σ. Ionic-conductivity measurements of NVPOF-M (M = Sc, V, Cr, and Fe) and pristine NVPOF reveal that heteroatom incorporation effectively reduces the bulk resistance (Fig. 2). Notably, NVPOF exhibits the highest bulk resistance, whereas NVPOF-Fe shows the lowest value, implying an enhanced ionic conductivity for NVPOF-Fe.

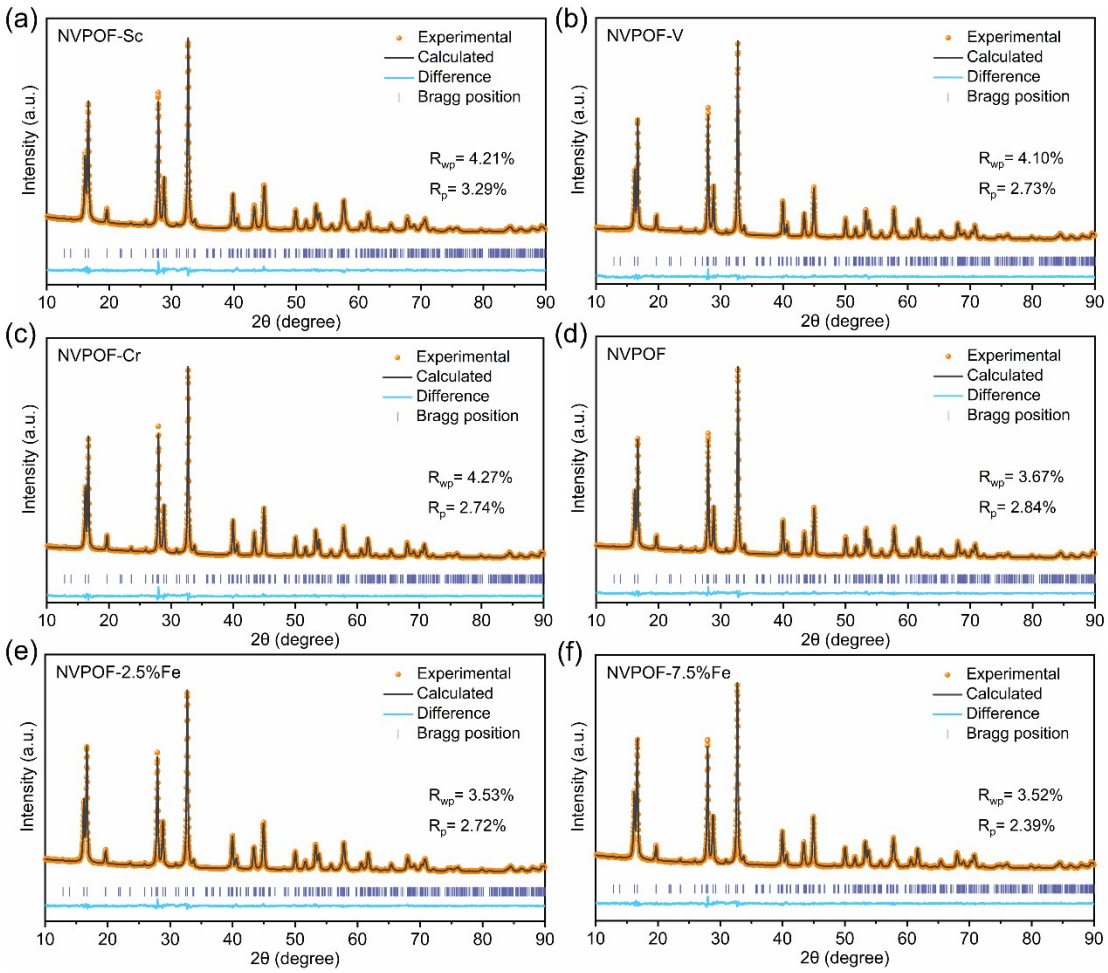


**Fig. S6.** XRD Rietveld refinement patterns of (a) NVPOF-Sc, (b) NVPOF-V, (c) NVPOF-Cr, (d) NVPOF, (e) NVPOF-2.5%Fe, and (f) NVPOF-7.5%Fe.

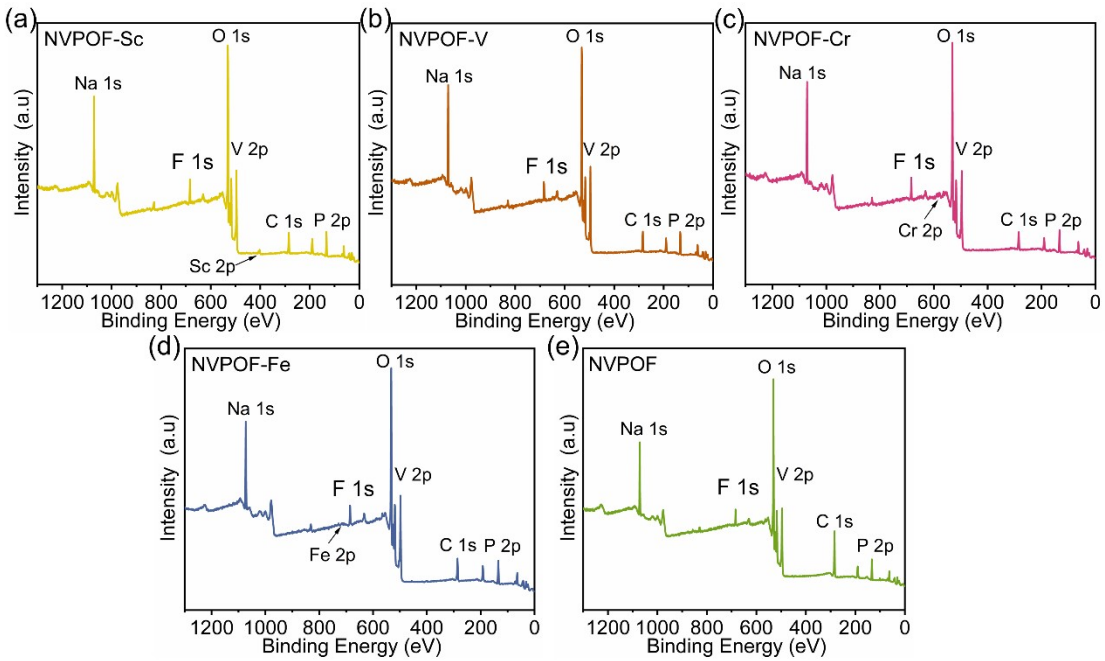


**Fig. S7.** XPS full spectrum of (a) NVPOF-Sc, (b) NVPOF-Cr, (c) NVPOF-V, (d) NVPOF Fe, and (e) NVPOF.

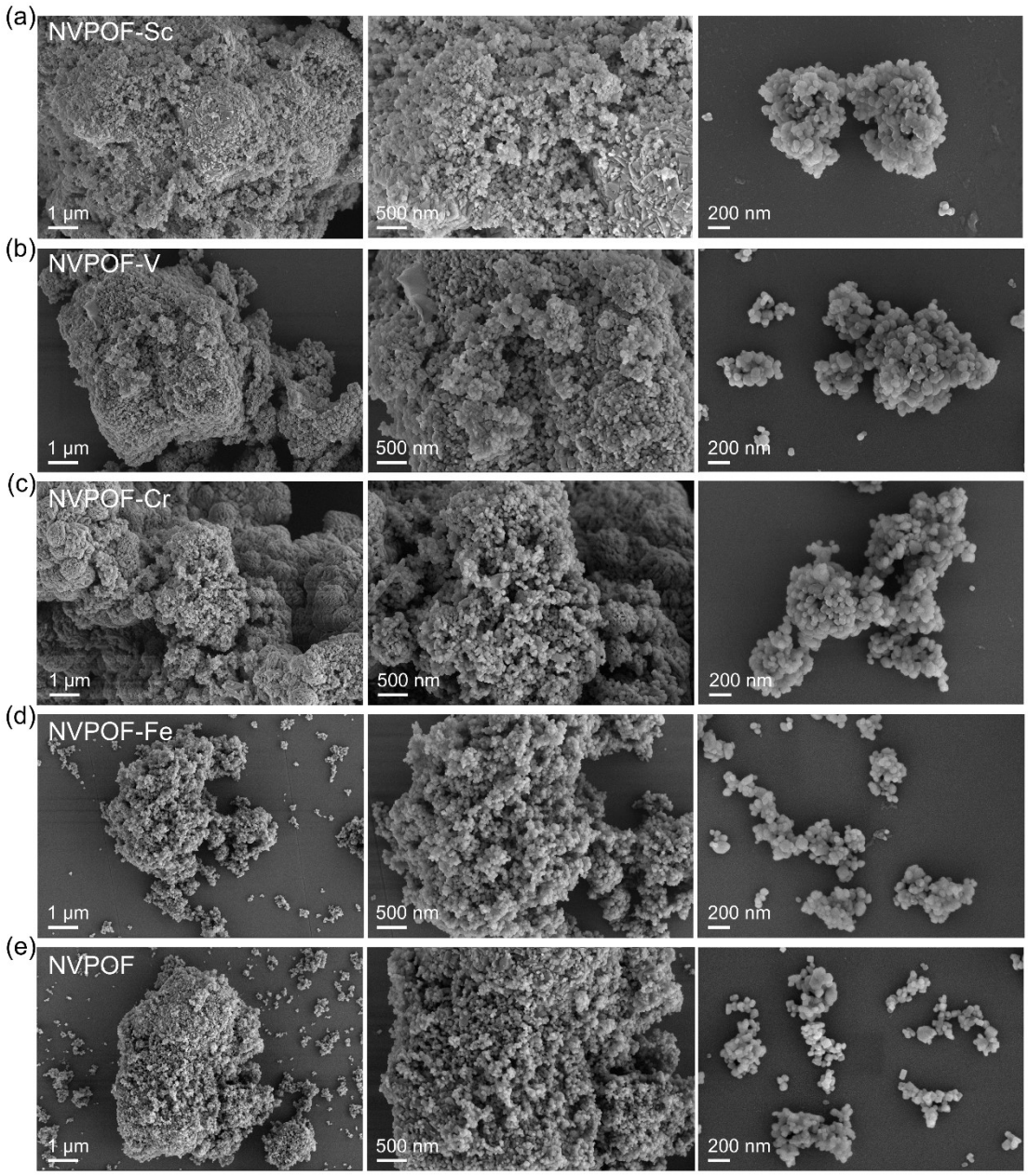


**Fig. S8.** The SEM images of (a) NVPOF-Sc, (b) NVPOF-V, (c) NVPOF-Cr, (d) NVPOF-Fe, and (e) NVPOF.

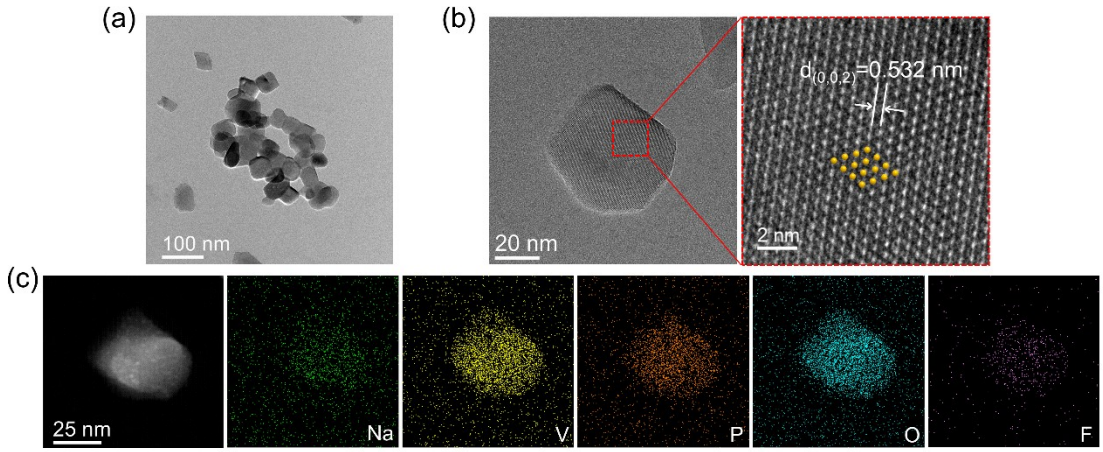


**Fig. S9.** (a) TEM, (b) HRTEM, and (c) EDS mapping of NVPOF.

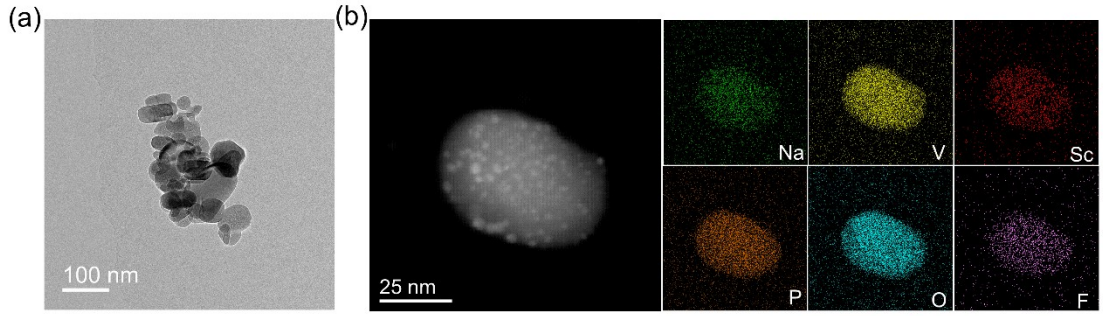


**Fig. S10.** (a) TEM and (b) EDS mapping of NVPOF-Sc.

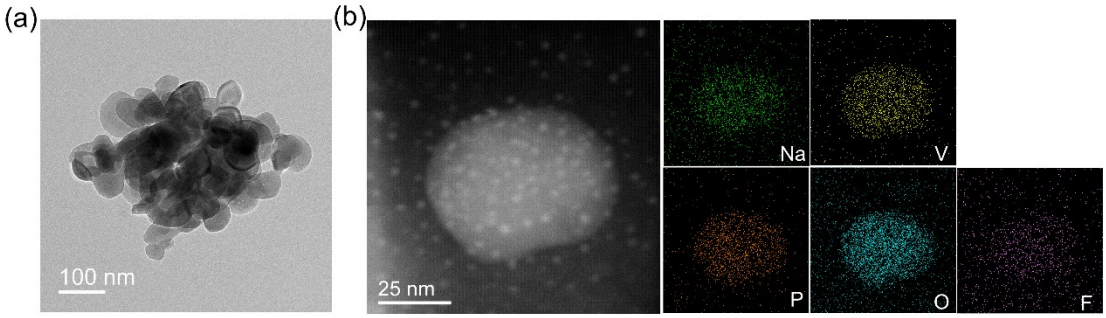


**Fig. S11.** (a) TEM and (b) EDS mapping of NVPOF-V.

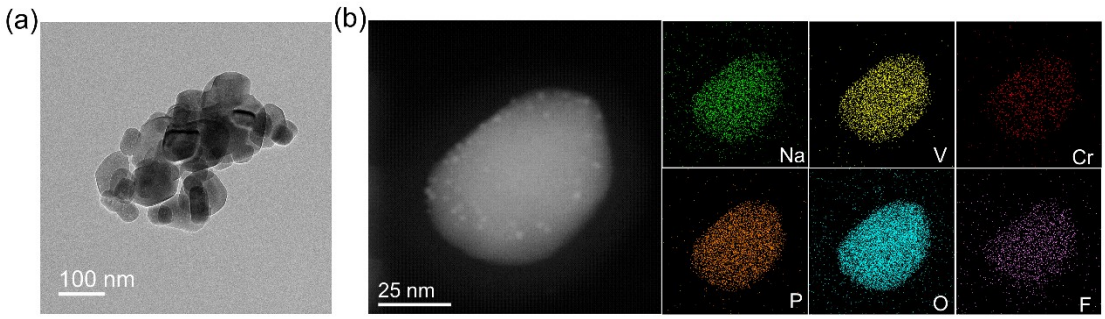


**Fig. S12.** (a) TEM and (b) EDS mapping of NVPOF-Cr.

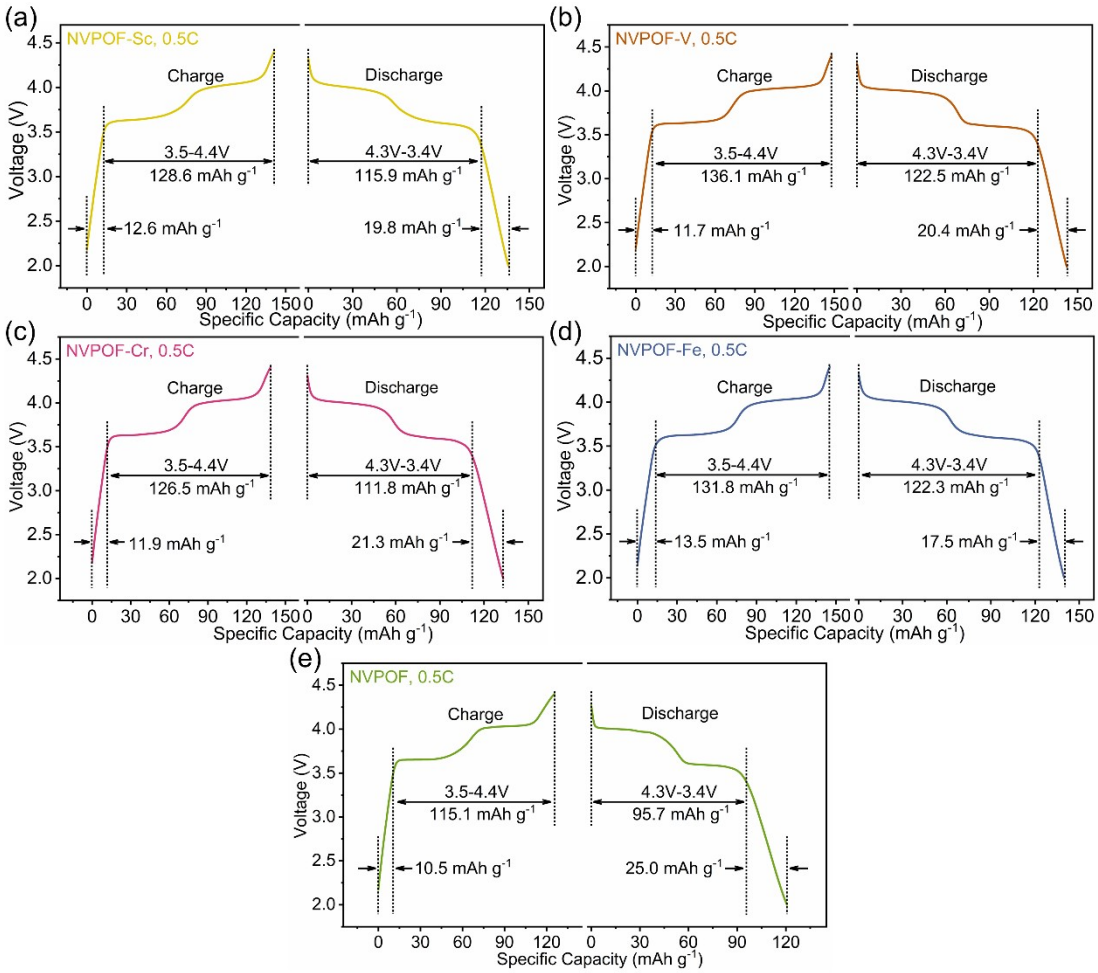


**Fig. S13.** The GCD curves of (a) NVPOF-Sc, (b) NVPOF-V, (c) NVPOF-Cr, (d) NVPOF-Fe, and (e) NVPOF at 0.5C**.**

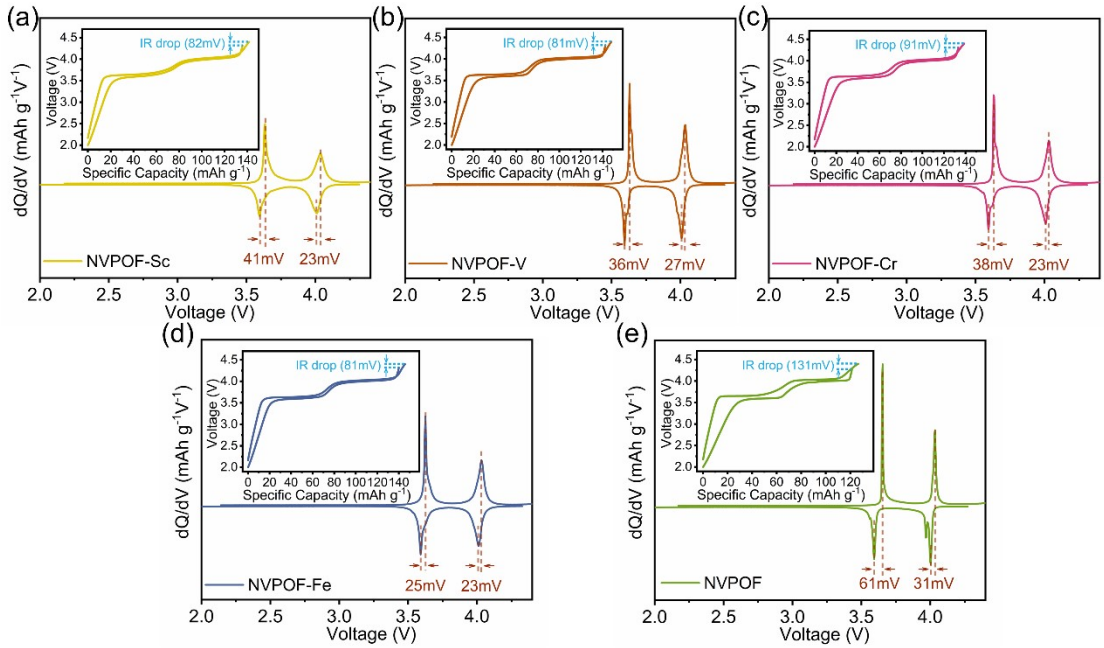


**Fig. S14.** The dQ/dV curves of a) NVPOF-Sc, (b) NVPOF-V, (c) NVPOF-Cr, (d) NVPOF-Fe, and (e) NVPOF at 0.5C (insets: Comparison of platform voltage difference and IR drop).

Note: The IR drop originates from changes in the internal resistance of the cell, including contributions from the electrolyte, the electrode material, the current collector, and the resistances associated with the conductive additive and binder. A pronounced IR drop is detrimental because it leads to energy loss, thereby lowering the overall efficiency, and it also generates heat that can raise safety concerns. Reducing these resistive is therefore an effective strategy to mitigate such adverse effects. Common approaches include applying conductive coatings on the surface of active materials and employing higher-performance conductive additives, both of which enhance electronic transport. According to the results of the four point probe electronic conductivity test, NVPOF-Fe exhibits the smallest IR drop, which can be attributed to the introduction of $Fe^{3+}$ that effectively improves the electronic conductivity of the material.

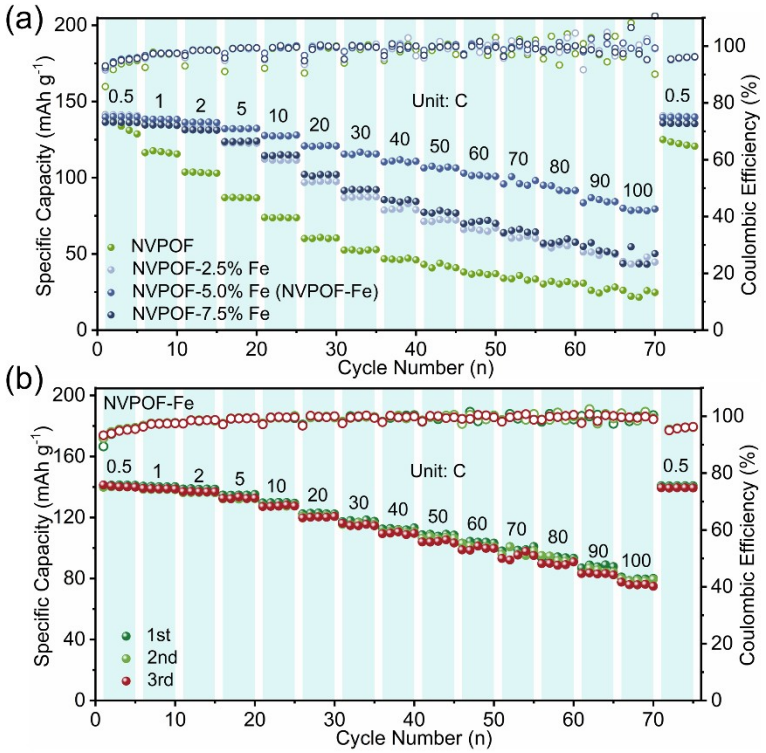


**Fig. S15.** (a) Rate performance of NVPOF and NVPOF-xFe (x = 2.5%, 5%, 7.5%), where NVPOF-5%Fe is referred to as NVPOF-Fe. (b) NVPOF-Fe rate performance of different synthetic batches..

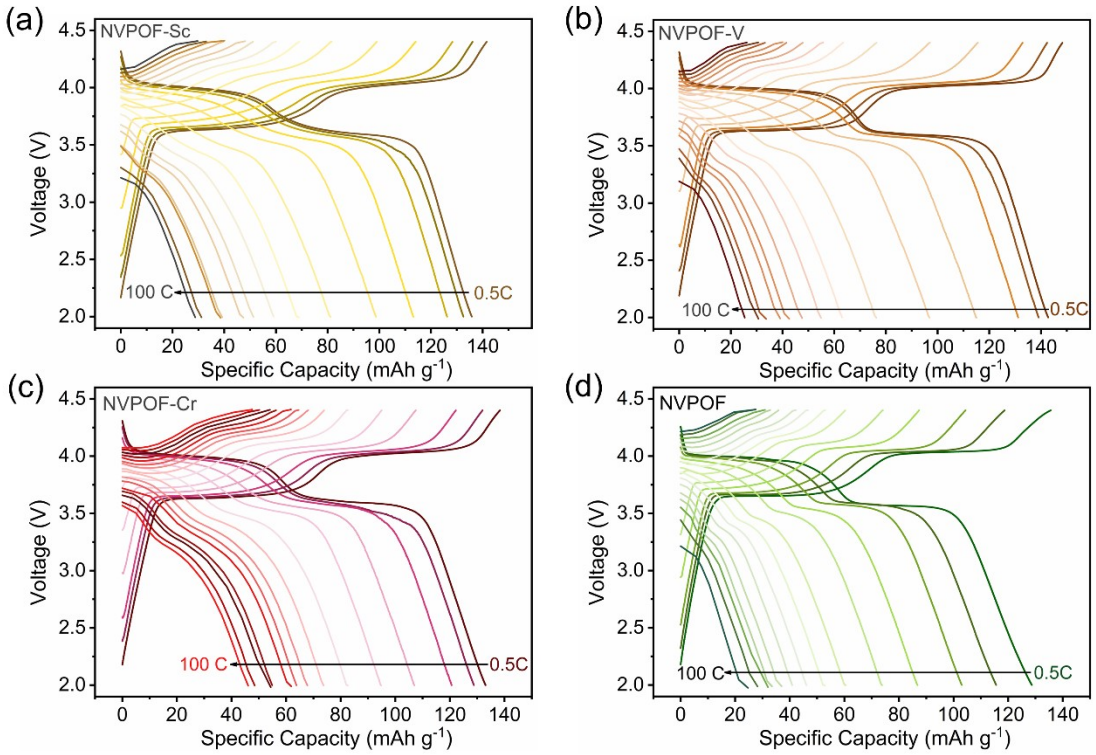


**Fig. S16.** The GCD curves of (a) NVPOF-Sc, (b) NVPOF-V, (c) NVPOF-Cr, and (d) NVPOF at different rate.

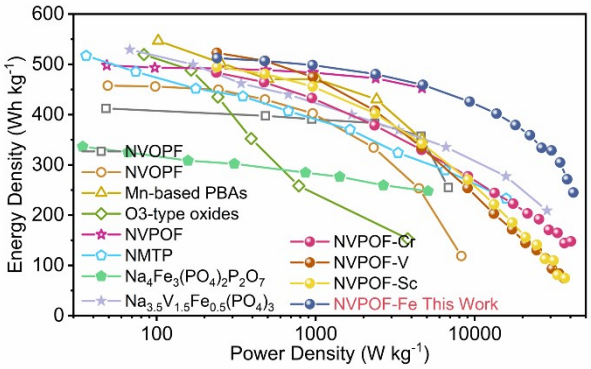


**Fig. S17.** Comparison of rate performance.

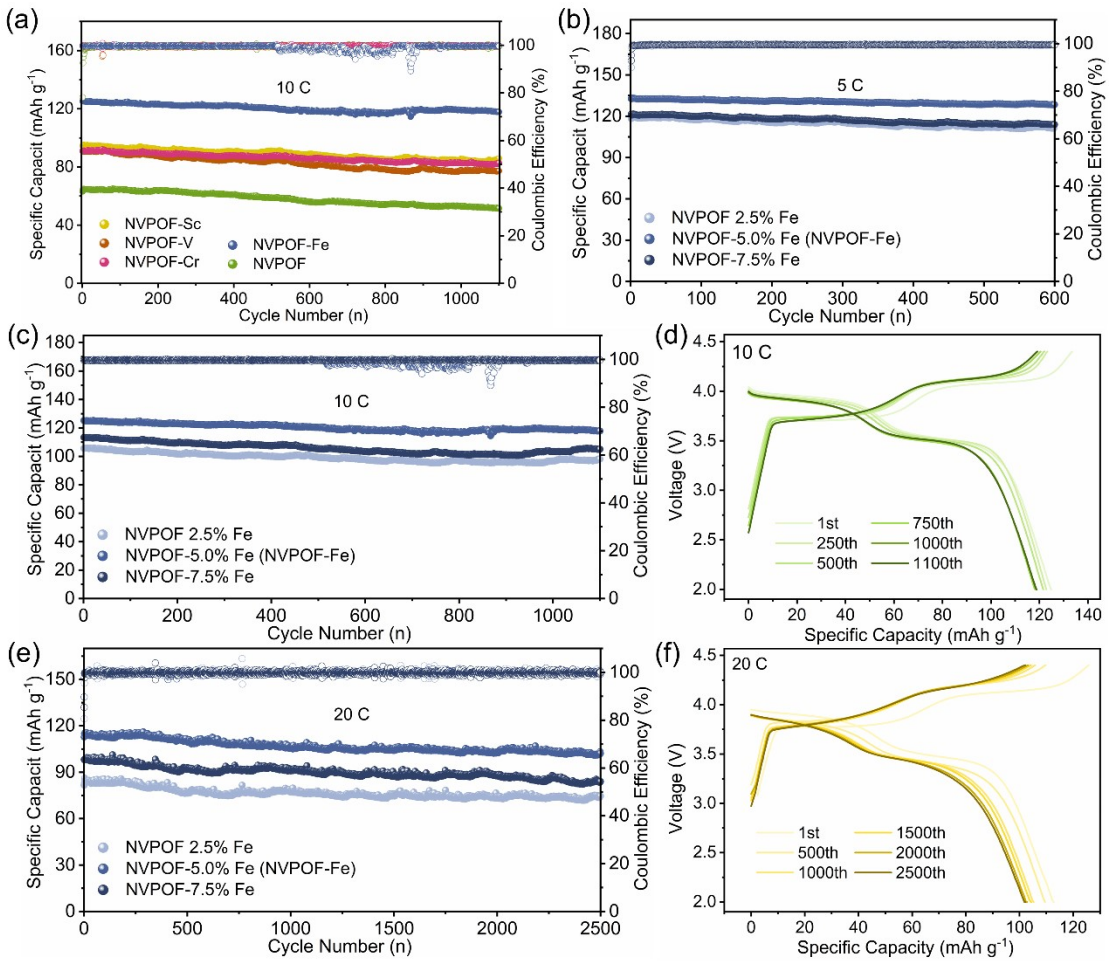


**Fig. S18.** (a) The cycling performances of NVPOF and NVPOF-M (M=Sc, V, Cr, and Fe) at 10C. The cyclic performance of NVPOF-xFe (x=2.5%, 5%, and 7.5%) at (b) 5C, (c) 10C, and (e) 20C, respectively. GCD curves of NVPOF-Fe at (d) 10C, and (f) 20C, respectively.

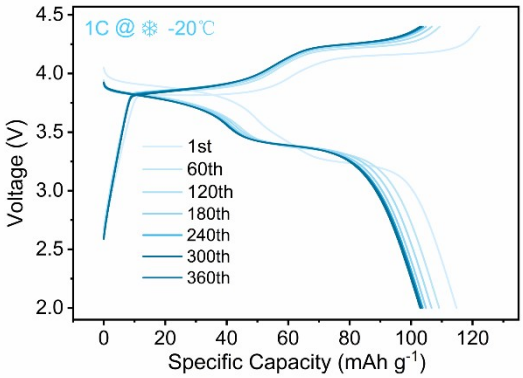


**Fig. S19.** The GCD curve of NVPOF-Fe cathode at 1C under －20° C.

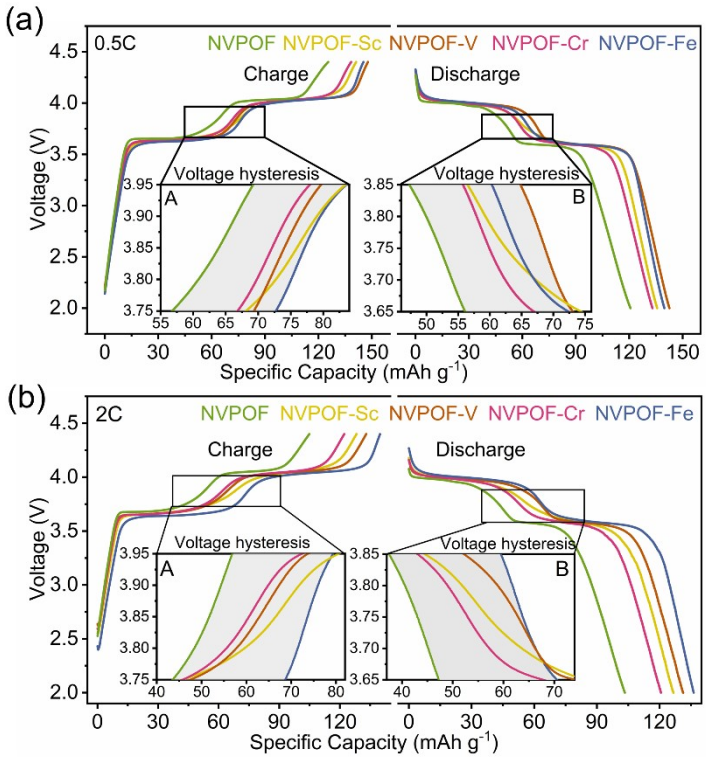


**Fig. S20.** Voltage profiles of NVPOF and NVPOF-M (M=Sc, V, Cr, and Fe) cathodes at 0.5C and 2C, respectively, insets: describes the voltage hysteresis of NVPOF cathode during charge/discharge process.

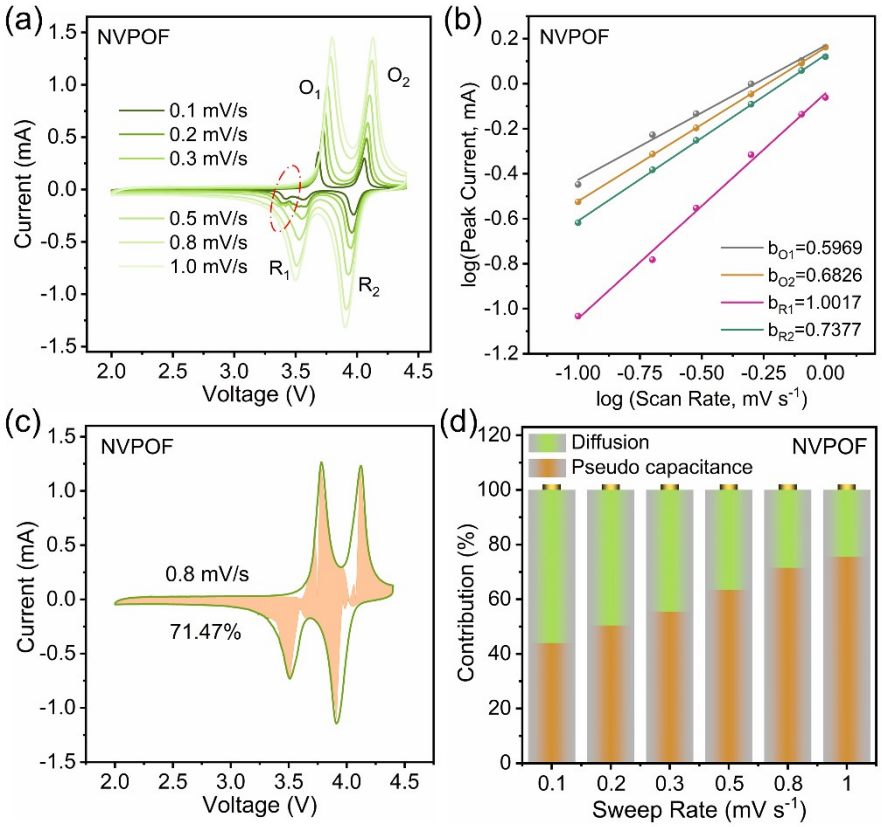


**Fig. S21.** Electrochemical performance of NVPOF cathode. (a) The CV curves of NVPOF at different scan rates and (b) the linear fitting profiles of the *log (i)* vs *log (v)* plots of O1, O2, R1, and R2. (c) Fitted pseudocapacitive contribution (orange area) of NVPOF electrode at 0.8 mV $s^{-1}$. (d) Proportions of pseudocapacitive (orange area) and diffusion-controlled (orange area) capacity of NVPOF cathode at different scanning rates.

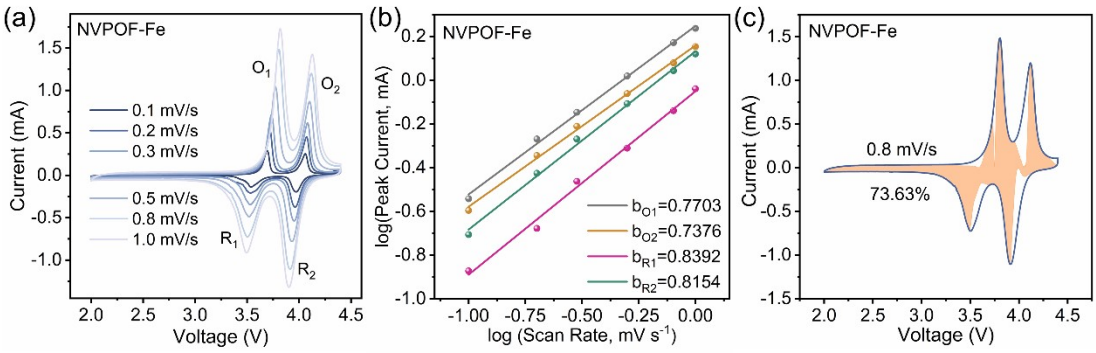


**Fig. S22.** Electrochemical performance of NVPOF-Fe cathode. (a) The CV curves of NVPOF at different scan rates and (b) the linear fitting profiles of the log (i) vs log (v) plots of O1, O2, R1, and R2. (c) Fitted pseudocapacitive contribution (orange area) of NVPOF electrode at 0.8 mV $s^{-1}$.

Calculate the diffusion coefficient of $Na^+$ ($D_{Na^+}$) based on the GITT curve using the following equation[12,13]:

$$D_{Na^+} = \frac{4}{\pi\tau}\left(\frac{m_B V_M}{M_B S}\right)^2\left(\frac{\Delta E_s}{\Delta E_\tau}\right)^2 \quad \text{(Supplementary Equation 1)}$$

Among them, $\tau$ refers to the constant current pulse time, $m_B$ is the mass, $V_M$ is the molar volume, $M_B$ is the molar mass, and $S$ is the electrode electrolyte interface area. $\triangle E_S$ is the voltage difference of one pulse relaxation period, and $\triangle E_\tau$ is the voltage difference of one constant current.

Discuss the charge storage mechanism of cathode materials based on the following equation[14]:

$$i_p = av^b \quad \text{(Supplementary Equation 2)}$$

$$logi_p = b \times logv + loga \quad \text{(Supplementary Equation 3)}$$

$$i_p = k_1 v + k_2 v^{1/2} \quad \text{(Supplementary Equation 4)}$$

Among them, $i_p$ is the peak current, $v$ is the scan rate, $a$ and $b$ are fitting parameters, and the value of b determines the type of electrochemical reaction. When $k \approx 0.5$, the electrochemical reaction is mainly controlled by diffusion; When $k \approx 1$, the electrochemical reaction is expressed as a pseudocapacitive response. $k_1$ and $k_2$ are fitting parameters, and if $i_p$ varies with $v^{1/2}$, then the electrochemical reaction is a

diffusion controlled redox reaction. If $i_p$ changes with $v$, the electrochemical reaction is a capacitive process controlled by charge transfer.

Note: As shown in Figure S21b, the R1 peak of NVPOF displays a distinct shoulder, leading to a reduced peak height and indicating the occurrence of side reactions. Consequently, the fitted b value exceeds 1(1.0017), implying that the fitting of the R1 peak is unreliable.

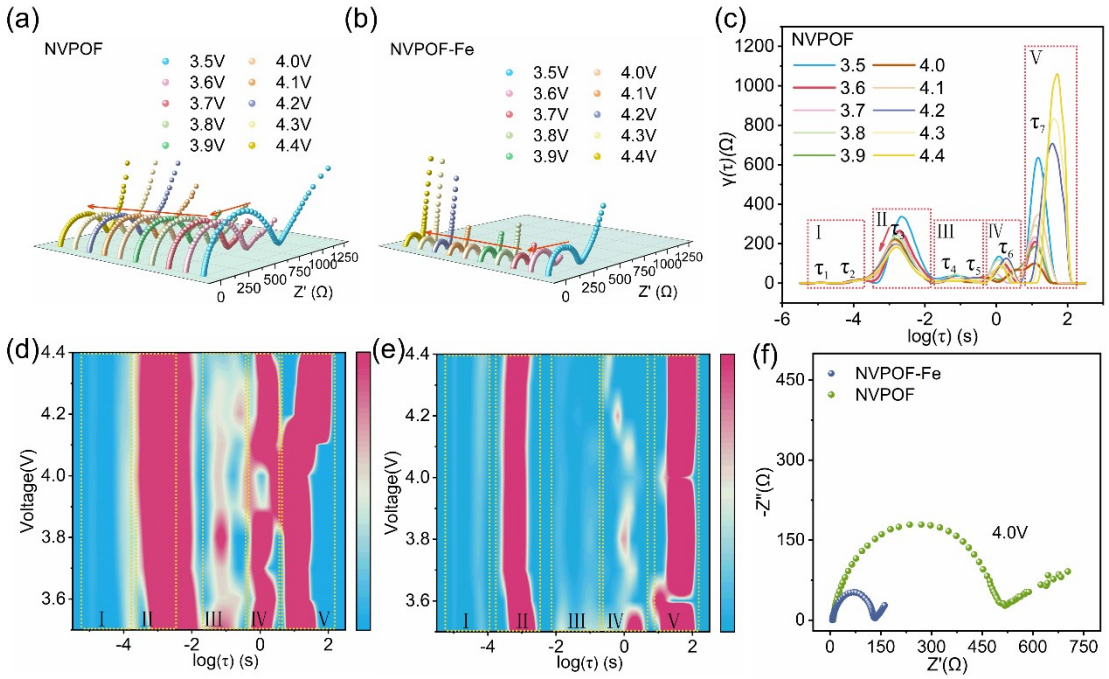


**Fig. S23.** EIS plots of (a) NVPOF and (b) NVPOF-Fe cathode at different potentials. (c) The DRT of NVPOF cathode at different potentials. The 2D contour plots of DRT for (d) NVPOF and (e) NVPOF-Fe cathode. Comparison of EIS of NVPOF and NVPOF-Fe cathodes at 4.0V.

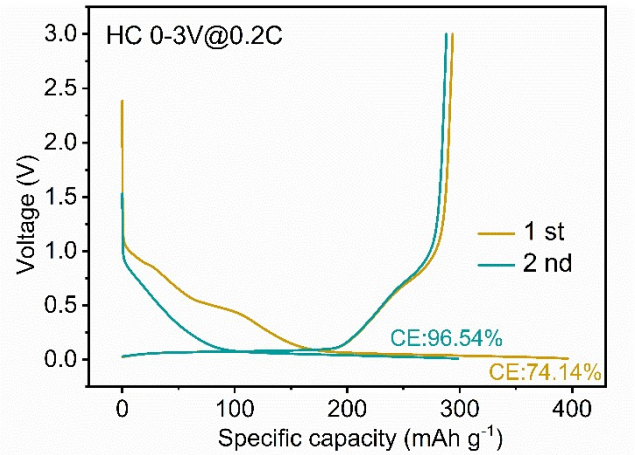


**Fig. S24.** The GCD curve of hard carbon (HC) in two cycles at 0.2C.

Note: Presodiation is widely regarded as one of the most practical approaches to compensate for the initial irreversible capacity. As shown in Fig. 1, HC delivers an ICE of 74.14% at 0.2C (1C=300mAh $g^{-1}$), which is far below the coulombic efficiency in the second cycle (96.54%). Therefore, presodiation is adopted to improve the coulombic efficiency of HC.

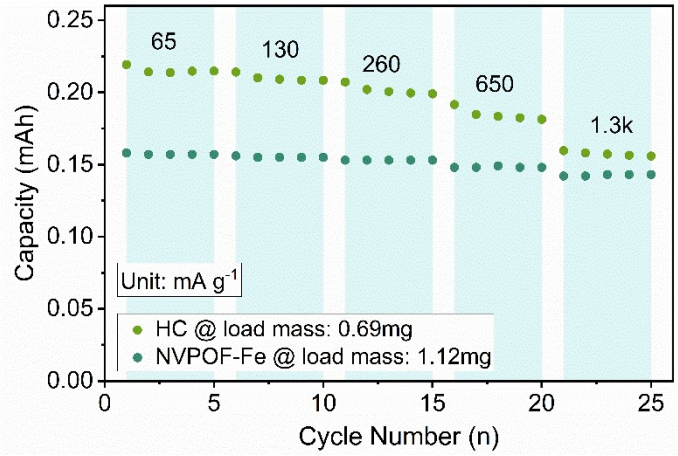


**Fig. S25.** Rate performance of NVPOF-Fe and HC.

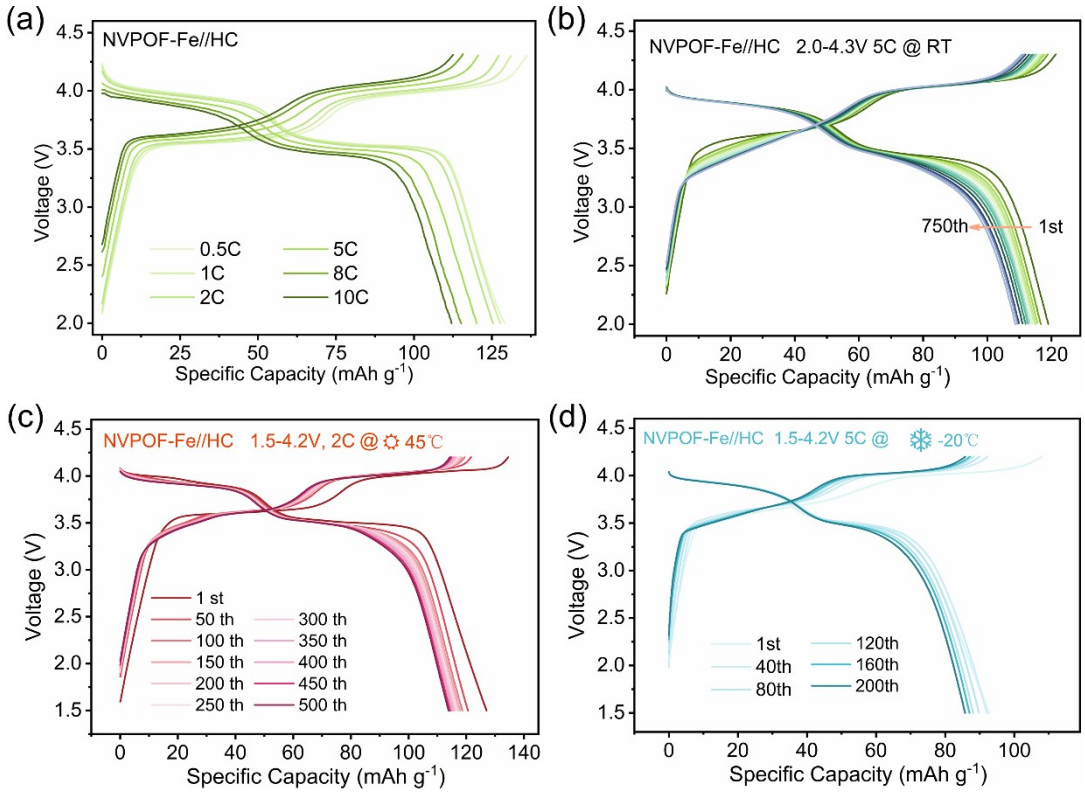


**Fig. S26.** Electrochemical performance of NVPOF Fe//HC full cell. (a) GCD curve corresponding to rate performance. (b) GCD curve corresponding to cycling performance at 5 C under room temperature. (c) GCD curve corresponding to cycling performance at 2C under 45°C. (d) GCD curve corresponding to cycling performance at 1C under -20°C.

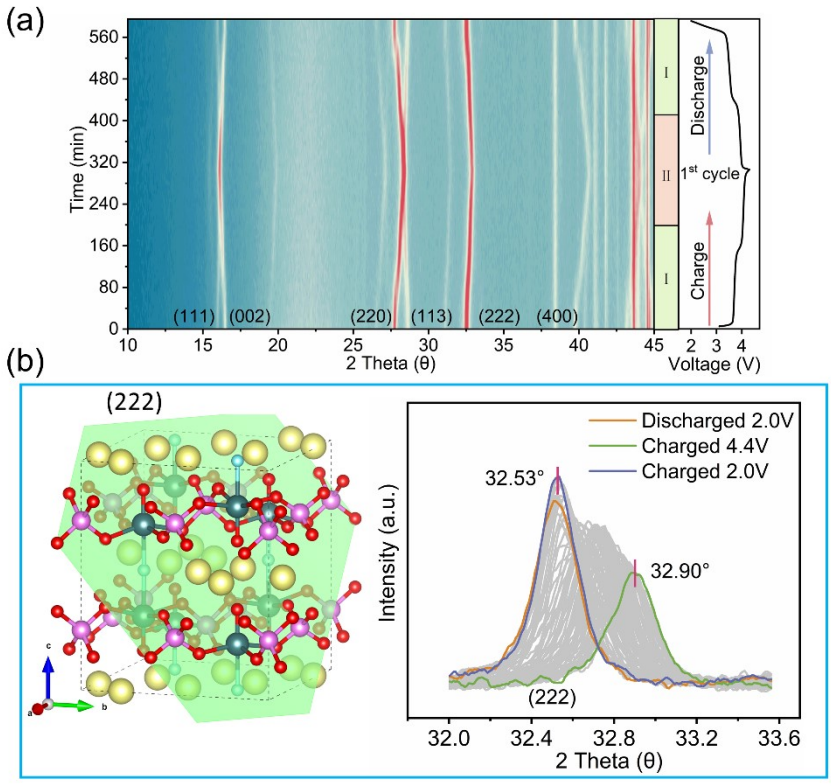


**Fig. S27.** (a) In situ XRD full patterns of NVPOF-Fe cathode. (b) In situ XRD patterns of (222) diffraction peaks of NVOPF-Fe cathode during charging/discharging process.

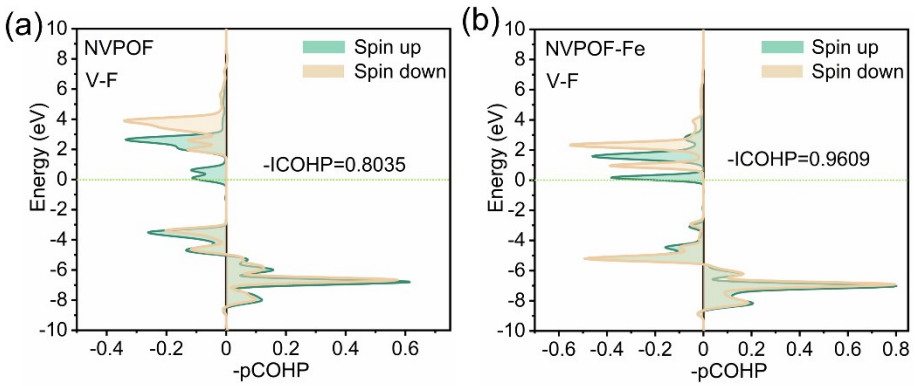


**Fig. S28.** The COHP profiles of V-F bond cooperation in (a) NVPOF and (b) NVPOF Fe based on DFT calculations.

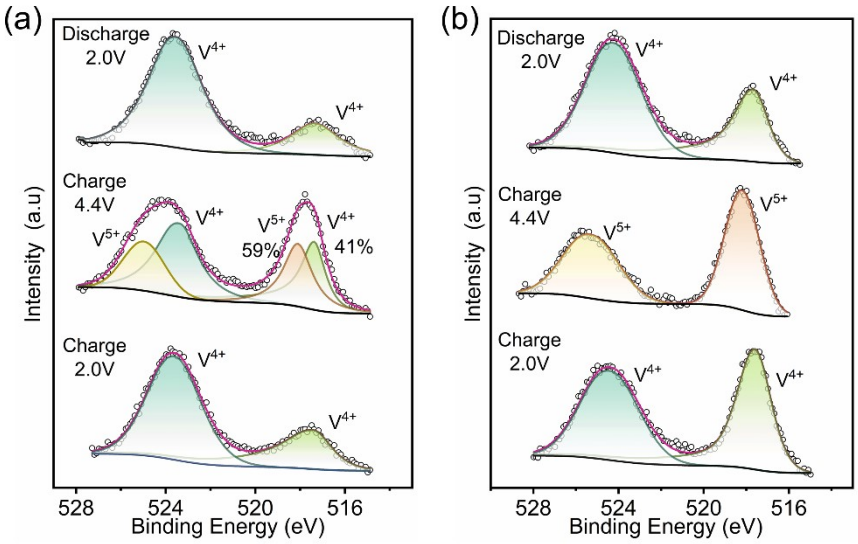


**Fig. S29.** Ex situ high-resolution V 2p XPS of (a) NVPOF and (b) NVPOF-Fe cathodes under 5C charge/discharge.

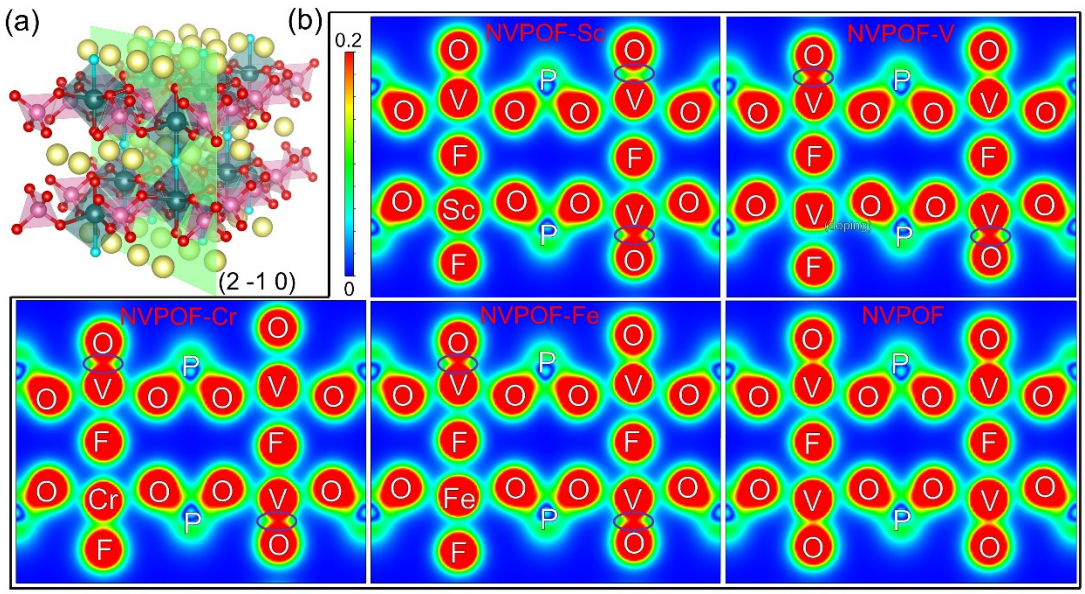


**Fig. S30.** (a) The schematic diagram of (2, -1, 0) crystal plane. (b) The charge density distribution of NVPOF and NVPOF-M (M=Sc, V, Cr, and Fe).

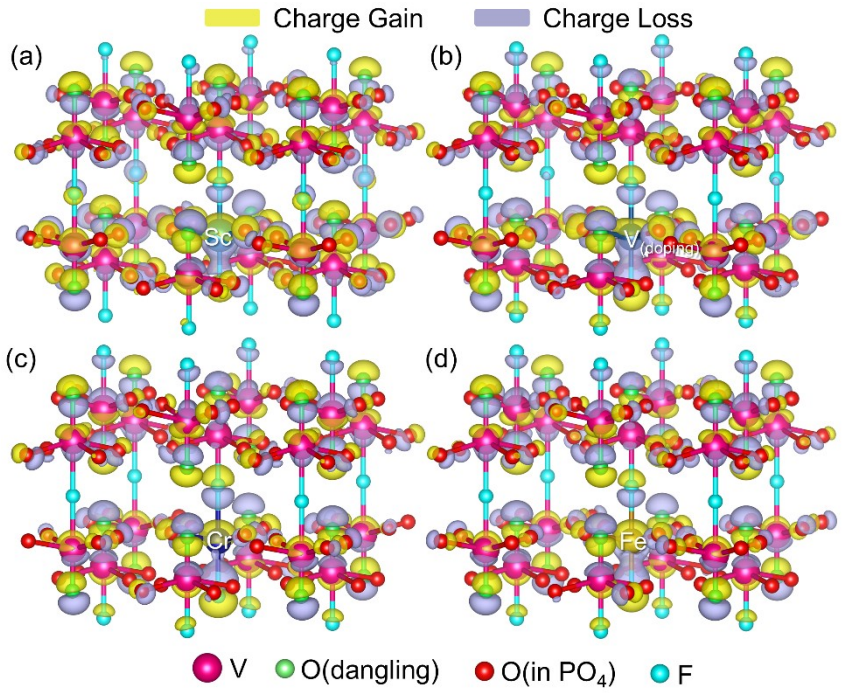


**Fig. S31.** The 3D charge difference of (a) NVPOF-Sc, (b) NVPOF-V, (c) NVPOF-Cr, and (d) NVPOF-Fe.

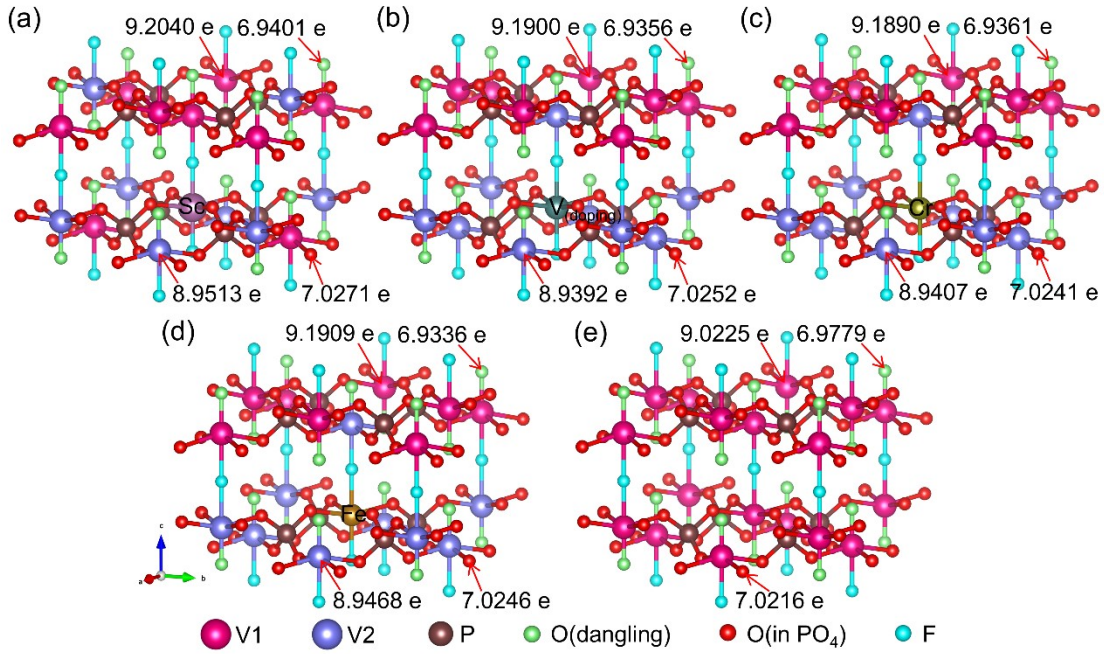


**Fig. S32.** The Bader charges of (a) NVPOF-Sc, (b) NVPOF-V, (c) NVPOF-Cr, (d) NVPOF-Fe, and (e) NVPOF.

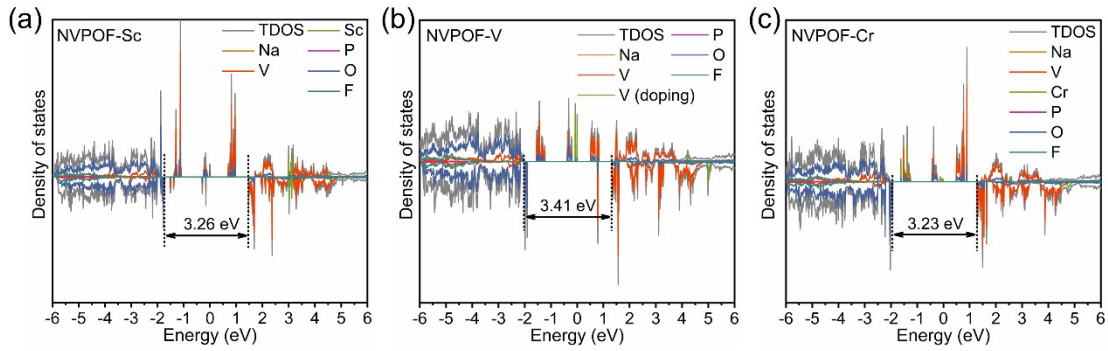


**Fig. S33.** The DOS for (a) NVPOF-Sc, (b) NVPOF-V, and (c) NVPOF-Cr.

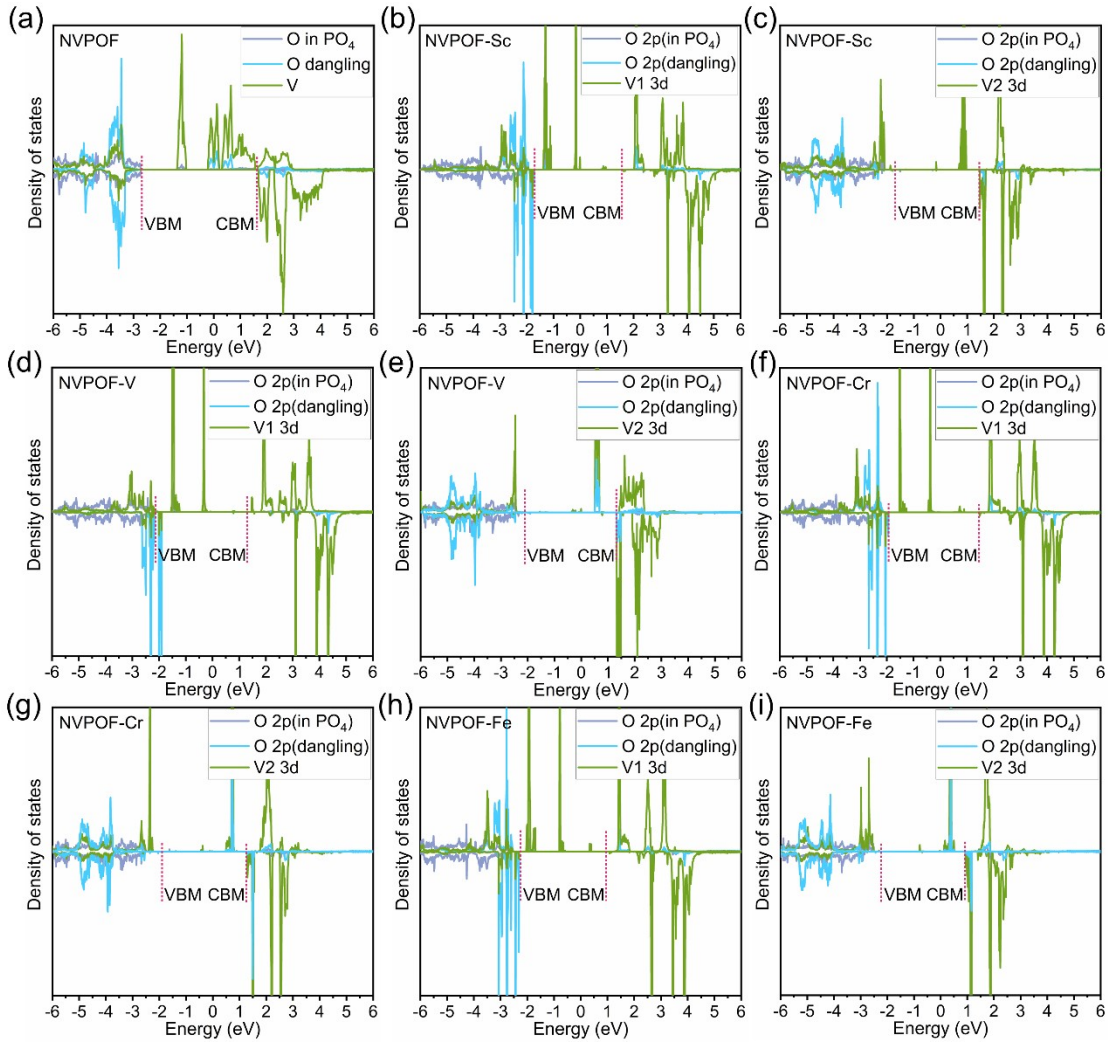


**Fig. S34.** The LDOS for (a) NVPOF, b-c) NVPOF-Sc, (d-e) NVPOF-V, (f-g) NVPOF-Cr, and (h-i) NVPOF-Fe.

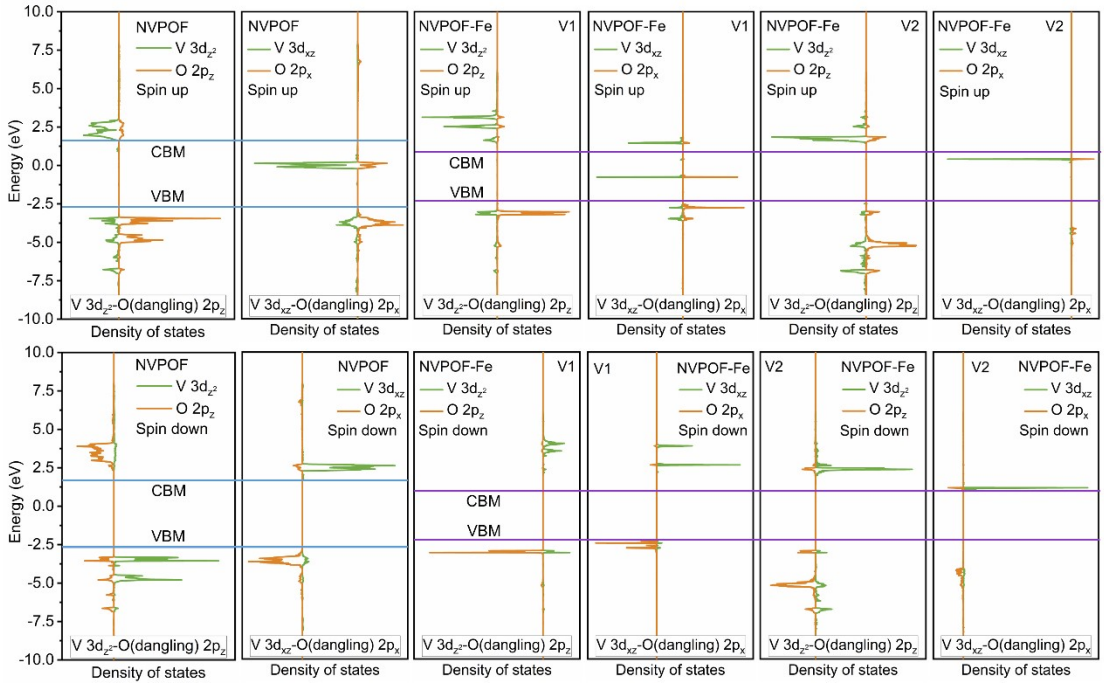


**Fig. S35.** The LDOS of V 3d and O(dangling) 2p orbitals of NVPOF and NVPOF-Fe.

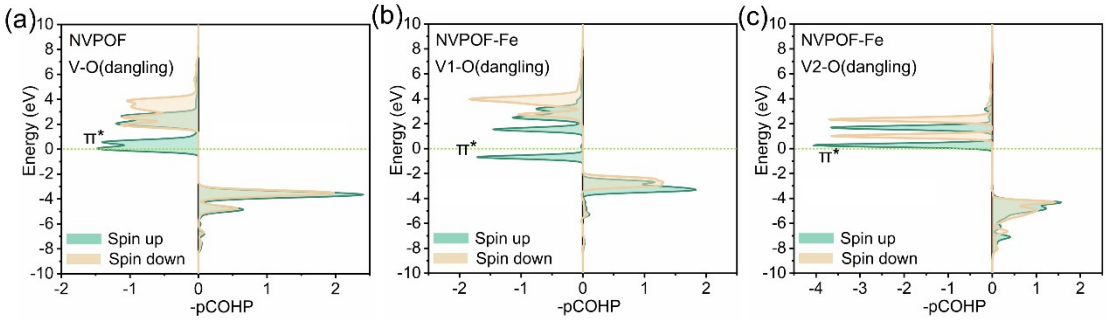


**Fig. S36.** (a) The COHP profiles for V-O bond of NVPOF. The COHP profiles for (b) V1-O(dangling) and (c) V2-O(dangling) bond of NVPOF-Fe.

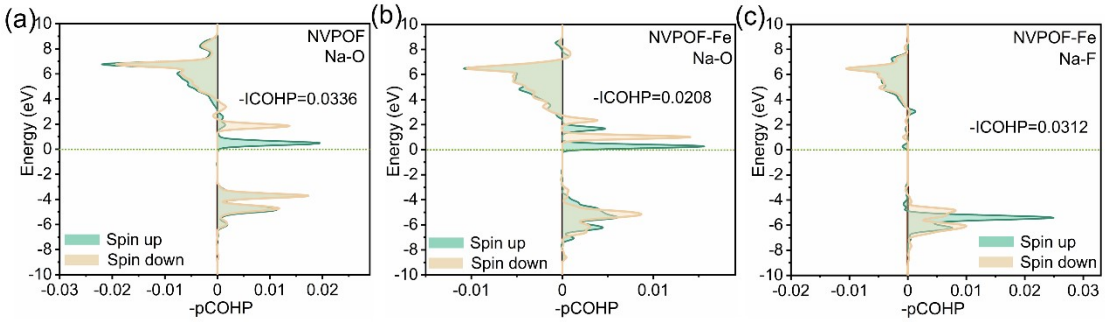


**Fig. S37.** (a) The COHP profiles for Na-O bond of NVPOF. The COHP profiles for (b) Na-O and (c) Na-F bond of NVPOF-Fe.

Note: In NVPOF, $Na^{+}$ reside within the pseudo-interlayer sites and coordinate with dangling oxygen atoms through Na–O bonds. When $V^{4+}$ is partially substituted by $Fe^{3+}$, dangling $O^{2-}$ are replaced by $F^{-}$ to preserve charge neutrality. As a result, NVPOF-Fe features $Na^{+}$ coordinated to both terminal oxygen and terminal fluorine atoms, forming Na-O and Na-F bonds, respectively.

**Table S1**. Comparison of energy density between NVPOF-M (M=Sc, V, Cr, and Fe) and advanced SIBs cathodes.

| Sample | Energy density | Ref. |
|---|---|---|
| HE-NMTP | 500 Wh $kg^{-1}$ at ~18 mA $g^{-1}$ | [15] |
| CZP-NVP | 378.21 Wh $kg^{-1}$ at 117 mA $g^{-1}$ | [16] |
| HE-NVP | 395.2 Wh $kg^{-1}$ at ~59 mA $g^{-1}$ | [17] |
| $NM_{1.7}FPP$/C-CNT | 383.8 Wh $kg^{-1}$at 13 mA $g^{-1}$ | [18] |
| $Na_3VFe(PO_4)_3$ | 305 Wh $kg^{-1}$ at ~ 59 mA $g^{-1}$ | [19] |
| NVMP-NSRs | 413.1 Wh $kg^{-1}$ at 55 mA $g^{-1}$ | [20] |
| HE-Cu | 396.1 Wh $kg^{-1}$ at 10 mA $g^{-1}$ | [21] |
| NMTP-$Na_{0.5}$ | 500 Wh $kg^{-1}$ at ~18 mA $g^{-1}$ | [22] |
| HE-NVP | 425 Wh $kg^{-1}$ at 50 mA $g^{-1}$ | [23] |
| NVFP | 501 Wh $kg^{-1}$ at 50 mA $g^{-1}$ | [24] |
| NVOPF-PE | 452 Wh $kg^{-1}$ at 13 mA $g^{-1}$ | [25] |
| $NVPOFSi_{0.05}$ | 480 Wh $kg^{-1}$ at 65 mA $g^{-1}$ | [26] |
| O3-NMNLCTO | 423.1 Wh $kg^{-1}$ at 10 mA $g^{-1}$ | [27] |
| **NVPOF-Sc** | **494.7 Wh $kg^{-1}$ at 65 mA $g^{-1}$** | **This Work** |
| **NVPOF-V** | **522.8 Wh $kg^{-1}$ at 65 mA $g^{-1}$** | **This Work** |
| **NVPOF-Cr** | **483.7 Wh $kg^{-1}$ at 65 mA $g^{-1}$** | **This Work** |
| **NVPOF-Fe** | **512.4 Wh $kg^{-1}$ at 65 mA $g^{-1}$** | **This Work** |

**Table S2**. Lattice parameters of NVPOF, NVPOF-xFe (M=2.5%, 5% and 7.5%) and NVPOF-M (M=Sc, V and Cr) obtained from XRD Rietveld refinements.

| Atom | a / Å | b / Å | c / Å | Volume / Å |
|---|---|---|---|---|
| NVPOF | 9.02229 | 9.02229 | 10.61736 | 864.272 |
| NVPOF-2.5%Fe | 9.02313 | 9.02313 | 10.62166 | 864.781 |
| NVPOF-5%Fe | 9.02165 | 9.02165 | 10.62662 | 864.899 |
| NVPOF-7.5%Fe | 9.02208 | 9.02208 | 10.62737 | 865.046 |
| NVPOF-Sc | 9.04704 | 9.04704 | 10.63163 | 870.188 |
| NVPOF-V | 9.02239 | 9.02239 | 10.62104 | 864.590 |
| NVPOF-Cr | 9.02234 | 9.02234 | 10.62019 | 864.511 |

**Table S3**. The refined crystallographic data of NVPOF obtained from XRD Rietveld refinements.

| Atom | Type | Wyckoff | X / a | Y / b | Z/ c | Occ. |
|---|---|---|---|---|---|---|
| Na1 | Na | 8 i | 0.5115 | 0.2395 | 0.0000 | 0.8410 |
| Na2 | Na | 8 i | 0.7951 | 0.0381 | 0.0000 | 0.7050 |
| V | V | 8 j | 0.24880 | 0.24880 | 0.19974 | 1.000 |
| P1 | P | 4 d | 0.0000 | 0.5000 | 0.2500 | 1.0000 |
| P2 | P | 4 e | 0.0000 | 0.0000 | 0.2514 | 1.0000 |
| O1 | O | 16 k | 0.0962 | 0.4087 | 0.1629 | 1.0000 |
| O2 | O | 8 j | 0.0980 | 0.0980 | 0.1622 | 1.0000 |
| O3 | O | 8 j | 0.4027 | 0.4027 | 0.1682 | 1.0000 |
| O4 | O | 8 j | 0.2520 | 0.2520 | 0.3528 | 1.0000 |
| F1 | F | 4 f | 0.2453 | 0.2453 | 0.0000 | 1.0000 |

**Table S4**. The refined crystallographic data of NVPOF-2.5%Fe obtained from XRD Rietveld refinements.

| Atom | Type | Wyckoff | X / a | Y / b | Z/ c | Occ. |
|---|---|---|---|---|---|---|
| Na1 | Na | 8 i | 0.5073 | 0.2401 | 0.0000 | 0.8120 |
| Na2 | Na | 8 i | 0.7940 | 0.0387 | 0.0000 | 0.7060 |
| V | V | 8 j | 0.2500 | 0.2500 | 0.1986 | 0.9750 |
| Fe | Fe | 8 j | 0.2500 | 0.2500 | 0.1986 | 0.0250 |
| P1 | P | 4 d | 0.0000 | 0.5000 | 0.2500 | 1.0000 |
| P2 | P | 4 e | 0.0000 | 0.0000 | 0.2521 | 1.0000 |
| O1 | O | 16 k | 0.0968 | 0.4064 | 0.1621 | 1.0000 |
| O2 | O | 8 j | 0.0973 | 0.0973 | 0.1638 | 1.0000 |
| O3 | O | 8 j | 0.4037 | 0.4037 | 0.1699 | 1.0000 |
| O4 | O | 8 j | 0.2457 | 0.2457 | 0.3503 | 0.9750 |
| F1 | F | 4 f | 0.2411 | 0.2411 | 0.0000 | 1.0000 |
| F2 | F | 8 j | 0.2457 | 0.2457 | 0.3503 | 0.0250 |

**Table S5**. The refined crystallographic data of NVPOF-5%Fe obtained from XRD Rietveld refinements.

| Atom | Type | Wyckoff | X / a | Y / b | Z/ c | Occ. |
|---|---|---|---|---|---|---|
| Na1 | Na | 8 i | 0.5085 | 0.2382 | 0.0000 | 0.8210 |
| Na2 | Na | 8 i | 0.7898 | 0.0414 | 0.0000 | 0.6910 |
| V | V | 8 j | 0.2502 | 0.2502 | 0.1985 | 0.9500 |
| Fe | Fe | 8 j | 0.2502 | 0.2502 | 0.1985 | 0.0500 |
| P1 | P | 4 d | 0.0000 | 0.5000 | 0.2500 | 1.0000 |
| P2 | P | 4 e | 0.0000 | 0.0000 | 0.2539 | 1.0000 |
| O1 | O | 16 k | 0.0985 | 0.4096 | 0.1624 | 1.0000 |
| O2 | O | 8 j | 0.0980 | 0.0980 | 0.1628 | 1.0000 |
| O3 | O | 8 j | 0.4035 | 0.4035 | 0.1704 | 1.0000 |
| O4 | O | 8 j | 0.2449 | 0.2449 | 0.3524 | 0.9500 |
| F1 | F | 4 f | 0.2428 | 0.2428 | 0.0000 | 1.0000 |
| F2 | F | 8 j | 0.2449 | 0.2449 | 0.3524 | 0.0500 |

**Table S6**. The refined crystallographic data of NVPOF-7.5%Fe obtained from XRD Rietveld refinements.

| Atom | Type | Wyckoff | X / a | Y / b | Z/ c | Occ. |
|---|---|---|---|---|---|---|
| Na1 | Na | 8 i | 0.5075 | 0.2435 | 0.0000 | 0.8470 |
| Na2 | Na | 8 i | 0.7973 | 0.0417 | 0.0000 | 0.6280 |
| V | V | 8 j | 0.2500 | 0.2500 | 0.1980 | 0.9250 |
| Fe | Fe | 8 j | 0.2500 | 0.2500 | 0.1980 | 0.0750 |
| P1 | P | 4 d | 0.0000 | 0.5000 | 0.2500 | 1.0000 |
| P2 | P | 4 e | 0.0000 | 0.0000 | 0.2573 | 1.0000 |
| O1 | O | 16 k | 0.0981 | 0.4073 | 0.1605 | 1.0000 |
| O2 | O | 8 j | 0.0974 | 0.0974 | 0.1703 | 1.0000 |
| O3 | O | 8 j | 0.4034 | 0.4034 | 0.1652 | 1.0000 |
| O4 | O | 8 j | 0.2438 | 0.2438 | 0.3514 | 0.9250 |
| F1 | F | 4 f | 0.2424 | 0.2424 | 0.0000 | 1.0000 |
| F2 | F | 8 j | 0.2438 | 0.2438 | 0.3514 | 0.0750 |

**Table S7**. The refined crystallographic data of NVPOF-Sc obtained from XRD Rietveld refinements.

| Atom | Type | Wyckoff | X / a | Y / b | Z/ c | Occ. |
|---|---|---|---|---|---|---|
| Na1 | Na | 8 i | 0.5184 | 0.2472 | 0.0000 | 0.8510 |
| Na2 | Na | 8 i | 0.7797 | 0.0267 | 0.0000 | 0.6980 |
| V | V | 8 j | 0.2491 | 0.2491 | 0.1980 | 0.9500 |
| Sc | Sc | 8 j | 0.2491 | 0.2491 | 0.1980 | 0.0500 |
| P1 | P | 4 d | 0.0000 | 0.5000 | 0.2500 | 1.0000 |
| P2 | P | 4 e | 0.0000 | 0.0000 | 0.2546 | 1.0000 |
| O1 | O | 16 k | 0.1015 | 0.4089 | 0.1621 | 1.0000 |
| O2 | O | 8 j | 0.0993 | 0.0993 | 0.1640 | 1.0000 |
| O3 | O | 8 j | 0.4097 | 0.4097 | 0.1718 | 1.0000 |
| O4 | O | 8 j | 0.2459 | 0.2459 | 0.3527 | 0.9500 |
| F1 | F | 4 f | 0.2581 | 0.2581 | 0.0000 | 1.0000 |
| F2 | F | 8 j | 0.2459 | 0.2459 | 0.3527 | 0.0500 |

**Table S8**. The refined crystallographic data of NVPOF-V obtained from XRD Rietveld refinements.

| Atom | Type | Wyckoff | X / a | Y / b | Z/ c | Occ. |
|---|---|---|---|---|---|---|
| Na1 | Na | 8 i | 0.5073 | 0.2428 | 0.0000 | 0.8470 |
| Na2 | Na | 8 i | 0.7846 | 0.0478 | 0.0000 | 0.6880 |
| V1 | V | 8 j | 0.2508 | 0.2508 | 0.1994 | 0.9500 |
| V2 | V | 8 j | 0.2508 | 0.2508 | 0.1994 | 0.0500 |
| P1 | P | 4 d | 0.0000 | 0.5000 | 0.2500 | 1.0000 |
| P2 | P | 4 e | 0.0000 | 0.0000 | 0.2512 | 1.0000 |
| O1 | O | 16 k | 0.0971 | 0.4095 | 0.1634 | 1.0000 |
| O2 | O | 8 j | 0.1005 | 0.1005 | 0.1634 | 1.0000 |
| O3 | O | 8 j | 0.4050 | 0.4050 | 0.1675 | 1.0000 |
| O4 | O | 8 j | 0.2403 | 0.2403 | 0.3533 | 0.9500 |
| F1 | F | 4 f | 0.2485 | 0.2485 | 0.0000 | 1.0000 |
| F2 | F | 8 j | 0.2403 | 0.2403 | 0.3533 | 0.0500 |

**Table S9**. The refined crystallographic data of NVPOF-Cr obtained from XRD Rietveld refinements.

| Atom | Type | Wyckoff | X / a | Y / b | Z/ c | Occ. |
|---|---|---|---|---|---|---|
| Na1 | Na | 8 i | 0.5132 | 0.2419 | 0.0000 | 0.8490 |
| Na2 | Na | 8 i | 0.7722 | 0.0341 | 0.0000 | 0.6710 |
| V1 | V | 8 j | 0.2500 | 0.2500 | 0.1990 | 0.9500 |
| Cr2 | Cr | 8 j | 0.2500 | 0.2500 | 0.1990 | 0.0500 |
| P1 | P | 4 d | 0.0000 | 0.5000 | 0.2500 | 1.0000 |
| P2 | P | 4 e | 0.0000 | 0.0000 | 0.2535 | 1.0000 |
| O1 | O | 16 k | 0.1007 | 0.4118 | 0.1595 | 1.0000 |
| O2 | O | 8 j | 0.0995 | 0.0995 | 0.1585 | 1.0000 |
| O3 | O | 8 j | 0.4064 | 0.4064 | 0.1767 | 1.0000 |
| O4 | O | 8 j | 0.2425 | 0.2425 | 0.3561 | 0.9500 |
| F1 | F | 4 f | 0.2534 | 0.2534 | 0.0000 | 1.0000 |
| F2 | F | 8 j | 0.2425 | 0.2425 | 0.3561 | 0.0500 |

**Table S10**. Summary of the rate performance and cycling performance of NVPOF cathodes.

| Sample | Voltage range | Rate performance | Cycle stability and capacity | Ref. |
|---|---|---|---|---|
| NVOPF/8%KB | 2.5-4.2V | 142.2 mAh $g^{-1}$ at 0.1C<br>112.8 mAh $g^{-1}$ at 20C | 98% after 10000 cycles at 20C<br>109.8 mAh $g^{-1}$ | [28] |
| $Na_{3-y}VPO_{2-x}Br_xF$ | 2.5-4.5V | 124.6 mAh $g^{-1}$ at 0.2C<br>77.7 mAh $g^{-1}$ at 50C | 94.4% after 800 cycles at 10C<br>109.7 mAh $g^{-1}$ | [29] |
| NVTC | 2.5-4.5V | 121.3 mAh $g^{-1}$ at 1C<br>78.5 mAh $g^{-1}$ at 30C | 96.88% after 3000 cycles at 20C<br>83.4mAhg−1 | [30] |
| NVPOF | 2.0-4.5V | 129.9 mAh $g^{-1}$ at 0.1C<br>99.9 mAh $g^{-1}$ at 20C | 80.2% after 5000 cycles at 20C<br>99.9 mAh $g^{-1}$ | [31] |
| NVMC-95 | 2.0-4.5V | 120 mAh $g^{-1}$ at 0.1C<br>99.9 mAh $g^{-1}$ at 20C | 76% after 2000 cycles at 5C<br>89 mAh $g^{-1}$ | [32] |
| $N_{0.92}K_{0.08}VPF/C$ | 2.5–4.3V | 128.8 mAh $g^{-1}$ at 0.2C<br>99.6 mAh $g^{-1}$ at 10C | 60.2% after 5000 cycles at 10C<br>68.2 mAh $g^{-1}$ | [33] |
| NVPOF-HE | 2.5–4.5V | 126.3 mAh $g^{-1}$ at 0.5C<br>73.9 mAh $g^{-1}$ at 50C | 91.2% after 4000 cycles at 10C<br>~95 mAh $g^{-1}$ | [34] |
| NVPF-Ti-0.05 | 2.0−4.3V | 129.1 mAh $g^{-1}$ at 0.2C<br>70.6 mAh $g^{-1}$ at 30C | 81.1% after 6000 cycles at 30C<br>70.62 mAh $g^{-1}$ | [35] |
| NVPOF-$Mg_{0.1}$ | 2.5−4.5V | 119.3 mAh $g^{-1}$ at 0.5C<br>75.9 mAh $g^{-1}$ at 60C | 96.3% after 500 cycles at 10C<br>~110 mAh $g^{-1}$ | [36] |
| $NVPOFSi_{0.05}$ | 2.0−4.3V | 125.8 mAh $g^{-1}$ at 0.5C<br>75.5 mAh $g^{-1}$ at 30C | 75% after 1000 cycles at 10C<br>110.3 mAh $g^{-1}$ | [26] |
| NVOPF-PE | 2.5−4.3V | 132 mAh $g^{-1}$ at 0.1C<br>129 mAh $g^{-1}$ at 10C | 81% after 6000 cycles at 10C<br>128.7 mAh $g^{-1}$ | [25] |
| **NVOPF-Fe** | **2.0−4.4V** | **139.8 mAh $g^{-1}$ at 0.5C<br>79.2 mAh $g^{-1}$ at 100C** | **90.6% after 2500 cycles at 20C<br>116 mAh $g^{-1}$** | **This Work** |

**Table S11**. Reaction kinetics of NVPOF-Fe cathode at various sweeping rates.

| Sweep Rate | Diffusion Ratio (%) | Pseudo Capacitance Ratio (%) |
|---|---|---|
| 0.1mV $s^{-1}$ | 55.65 | 44.35 |
| 0.2mV $s^{-}$ | 48.79 | 51.21 |
| 0.3mV $s^{-1}$ | 45.64 | 54.36 |
| 0.5 mV $s^{-1}$ | 33.85 | 66.15 |
| 0.8 mV $s^{-1}$ | 24.66 | 75.34 |
| 1 mV $s^{-1}$ | 21.12 | 78.83 |

**Table S12**. Reaction kinetics of NVPOF cathode at various sweeping rates.

| Sweep Rate | Diffusion Ratio (%) | Pseudo Capacitance Ratio (%) |
|---|---|---|
| 0.1mV $s^{-1}$ | 54.33 | 45.67 |
| 0.2mV $s^{-}$ | 47.90 | 52.10 |
| 0.3mV $s^{-1}$ | 42.79 | 57.21 |
| 0.5 mV $s^{-1}$ | 34.78 | 65.22 |
| 0.8 mV $s^{-1}$ | 26.72 | 73.28 |
| 1 mV $s^{-1}$ | 22.66 | 77.34 |

## Reference


1. Rodríguez-Carvajal, Recent advances in magnetic structure determination by neutron powder diffraction, *Phys. B*, 1993, **192**, 55-69.
2. K. Momma and F. Izumi, VESTA 3 for three-dimensional visualization of crystal, volumetric and morphology data, *J. Appl. Crystallogr.*, 2011, **44**, 1272-1276.
3. G. Kresse and D. Joubert, From ultrasoft pseudopotentials to the projector augmented-wave method, *Phys. Rev. B*, 1999, **59**, 1758.
4. J. P. Perdew, K. Burke and M. Ernzerhof, Generalized gradient approximation made simple, *Phys. Rev. Lett.*, 1996, **77**, 3865.
5. J. P. Perdew, M. Ernzerhof and K. Burke, Rationale for mixing exact exchange with density functional approximations, *J. Chem. Phys.*, 1996, **105**, 9982-9985.
6. N. E. Kirchner-Hall, W. N. Zhao, Y. H. Xiong, I. Timrov and I. Dabo, Extensive Benchmarking of DFT plus U Calculations for Predicting Band Gaps, *Appl. Sci.-Basel*, 2021, **11**, 2395.
7. Y. U. Park, D. H. Seo, H. Kim, J. Kim, S. Lee, B. Kim and K. Kang, A Family of High-Performance Cathode Materials for Na-ion Batteries, $Na_3(VO_{1-x}PO_4)_2F_{1+2x}$ ($0 \leq x \leq 1$): Combined First-Principles and Experimental Study, *Adv. Funct. Mater.*, 2014, **24**, 4603-4614.
8. W. Zhang, Y. L. Wu, Z. M. Xu, H. X. Li, M. Xu, J. W. Li, Y. H. Dai, W. Zong, R. W. Chen, L. He, Z. Zhang, D. J. L. Brett, G. J. He, Y. Q. Lai and I. P. Parkin, Rationally Designed Sodium Chromium Vanadium Phosphate Cathodes with Multi-Electron Reaction for Fast-Charging Sodium-Ion Batteries, *Adv. Energy Mater.*, 2022, **12**, 2201065.
9. Y. K. Xi, X. X. Wang, H. Wang, M. J. Wang, G. J. Wang, J. Q. Peng, N. J. Hou, X. Huang, Y. Y. Cao, Z. H. Yang, D. Z. Liu, X. H. Pu, G. Q. Cao, R. X. Duan, W. B. Li, J. J. Wang, K. Zhang, K. H. Xu, J. J. Zhang and X. F. Li, Optimizing the Electron Spin States of $Na_4Fe_3(PO_4)_2P_2O_7$ Cathodes via Mn/F Dual-Doping for Enhanced Sodium Storage, *Adv. Funct. Mater.*, 2024, **34**, 2315318.
10. S. Maintz, V. L. Deringer, A. L. Tchougréeff and R. Dronskowski, LOBSTER: A Tool to Extract Chemical Bonding from Plane-Wave Based DFT, *J. Comput. Chem.*, 2016, **37**, 1030-1035.
11. G. Henkelman, B. P. Uberuaga and H. Jónsson, A climbing image nudged elastic band method for finding saddle points and minimum energy paths, *J. Chem. Phys.*, 2000, **113**, 9901-9904.
12. W. Weppner and R. A. Huggins, Determination of the Kinetic Parameters of Mixed-Conducting Electrodes and Application to the System $Li_3Sb$, *J. Electrochem. Soc.*, 1977, DOI: 10.1149/1.2133112, 1569.
13. X. H. Rui, N. Ding, J. Liu, C. Li and C. H. Chen, Analysis of the chemical diffusion coefficient of lithium ions in $Li_3V_2(PO_4)_3$ cathode material, *Electrochim. Acta*, 2010, **55**, 2384-2390.
14. T. Brezesinski, J. Wang, S. H. Tolbert and B. Dunn, Ordered mesoporous α-$MoO_3$ with iso-oriented nanocrystalline walls for thin-film pseudocapacitors, *Nat. Mater.*, 2010, **9**, 146-151.
15. N. Zhang, X. R. Dong, Q. Yan, J. Y. Wang, F. Jin, J. X. Liu, D. L. Wang, H. K. Liu, B. Wang and S. X. Dou, High-entropy doping NASICON-Cathode breaks the kinetic barriers and suppresses voltage hysteresis for sodium ion batteries, *Energy Storage Mater.*, 2024, **72**, 103734.
16. H. D. Dong, C. C. Liu, Q. Huang, L. Guo and Y. J. Chen, Charge accumulation in carbon skeleton inducing oxygen vacancy-rich $Na_3V_2(PO_4)_3$ with multielectron transport property for high performance sodium ion batteries, *Energy Storage Mater.*, 2025, **75**, 104070.

17. X. Y. Liao, X. Wu, M. Xie, X. Y. Li, Y. J. Li, Z. D. Fu, G. H. Su, C. Q. Fang, H. Zhang, Q. J. Zheng, J. X. Zhao, B. Xu and D. M. Lin, Leveraging high-entropy substitution to achieve $V^{4+}/V^{5+}$ redox couple and superior Na+ storage in $Na_3V_2(PO_4)_3$-based cathodes for sodium-ion battery, *Energy Storage Mater.*, 2025, **77**, 104166.
18. X. Bao, Y. Wang, G. K. Chen, N. N. Qin, X. Wang, Y. J. He, Y. K. Shen, L. W. Chen, Y. X. Zhang, G. J. Cui, Z. F. Ma and X. Z. Liao, Unveiling the Key Factors: Mn/Fe Ratio, Distribution Homogeneity, and Electronic Conductivity of $Na_4Mn_xFe_{3-x}(PO_4)_2P_2O_7$ for Practical Sodium-Ion Batteries, *Adv. Funct. Mater.*, 2025, **35**, 2506242.
19. E. H. Wang, C. L. Xu, M. Z. Chen, W. B. Hua, X. H. Liu, Y. M. Liu, Z. G. Wu, Y. Xiao, W. Q. Yang, X. D. Guo and W. H. Chen, Superstructure Engineering Enables NASICON-Type Phosphate Cathodes with Increased Working Voltage and Energy Density, *Adv. Mater.*, 2025, **37**, e12435.
20. J. W. Zhao, B. Zou, W. T. Yan, S. J. Li, W. T. Wu, W. H. Wang, S. Y. Li and Y. Bai, Accelerating Electrochemical Responses of $Na_4VMn(PO_4)_3$ via Bulk-Defects and Architecture Engineering for High-Performance Sodium-Ion Batteries, *Adv. Sci.*, 2025, **12**, 2415331.
21. S. K. Chong, B. H. Lv, S. Y. Qiao, K. Yao, L. L. Yuan, Z. Q. Liu, H. K. Liu, S. X. Dou and W. Huang, Decoupling Roles of Cationic Dimensionality and Valence-Electron Compatibility on Structural Resilience and Kinetics in High-Entropy Prussian Blue Cathodes for Sodium-Ion Storage, *Angew. Chem., Int. Ed.*, 2025, **64**, e202512894.
22. S. P. Deng, M. R. Yang, Y. C. Wang, S. S. Cheng, S. Y. Li, L. Gu and Y. Bai, Regulating Na/Mn Antisite Defects and Revitalizing Reversible Redox Reactions in Phosphate Cathodes, *Acs Nano*, 2025, **19**, 30010-30020.
23. Z. Q. Hao, X. Y. Shi, W. Q. Zhu, Z. Yang, X. Z. Zhou, C. C. Wang, L. Li, W. B. Hua, C. Q. Ma and S. L. Chou, Boosting Multielectron Reaction Stability of Sodium Vanadium Phosphate by High-Entropy Substitution, *Acs Nano*, 2024, **18**, 9354-9364.
24. Y. F. Zhou, G. F. Xu, J. D. Lin, Y. P. Zhang, G. Z. Fang, J. Zhou, X. X. Cao and S. Q. Liang, Reversible Multielectron Redox Chemistry in a NASICON-Type Cathode toward High-Energy-Density and Long-Life Sodium-Ion Full Batteries, *Adv. Mater.*, 2023, **35**, 2304428.
25. C. L. Xu, Q. Fu, W. B. Hua, Z. Chen, Q. H. Zhang, Y. Bai, C. Yang, J. M. Zhao and Y. S. Hu, Overcoming Kinetic Limitations of Polyanionic Cathode toward High-Performance Na-Ion Batteries, *Acs Nano*, 2024, **18**, 18758-18768.
26. H. Zhou, Z. T. Cao, Y. F. Zhou, J. X. Li, Z. H. Ling, G. Z. Fang, S. Q. Liang and X. X. Cao, Unlocking rapid and robust sodium storage of fluorophosphate cathode via multivalent anion substitution, *Nano Energy*, 2023, **114**, 108604.
27. L. C. Li, T. T. Liu, M. H. Ding, H. H. Yu, Z. Dou, L. X. Wang, Weng, X. Z. Wu, J. Zhou and P. F. Zhou, Structural Modulation for Ultrastable O3-Type Layered Oxide Cathode Material of Sodium-Ion Batteries, *Adv. Funct. Mater.*, 2025, DOI: 10.1002/adfm.202514832, e14832.
28. X. Shen, Q. Zhou, M. Han, X. G. Qi, B. Li, Q. Q. Zhang, J. M. Zhao, C. Yang, H. Z. Liu and Y. S. Hu, Rapid mechanochemical synthesis of polyanionic cathode with improved electrochemical performance for Na-ion batteries, *Nat. Commun.*, 2021, **12**, 2848.
29. J. J. Wang, H. B. Jing, X. M. Wang, Y. Q. Xue, Q. H. Liang, W. H. Qi, H. Yu and C. F. Du, Electrostatically Shielded Transportation Enabling Accelerated $Na^+$ Diffusivity in High-Performance Fluorophosphate Cathode for Sodium-Ion Batteries, *Adv. Funct. Mater.*, 2024, **34**, 2315318.

30. X. Y. Wang, Z. X. Sun, W. Lv, Z. H. Zhan, M. Huang, Q. Wang, F. Zhang, H. Wang and X. J. Liu, Advanced Multifunctional Sodium-Ion Battery with High Current Conversion, Long Cycle Life, and All-Climate Temperature Range by Dual-Multivalent Cation Doping Strategy, *Adv. Energy Mater.*, 2025, **15**.
31. S. Q. Li, X. Y. Lu, Y. Li, H. Z. Wang, Y. F. Sun, Q. N. Zhou, J. S. Yue, R. Q. Guo, F. Wu, C. Wu and Y. Bai, Dynamic Lock-And-Release Mechanism Enables Reduced ΔG at Low Temperatures for High-Performance Polyanionic Cathode in Sodium-Ion Batteries, *Adv. Mater.*, 2024, **36**, 2413013.
32. M. Zaid, M. Karuppusamy, B. Patra, K. K. Garlapati, N. A. Murugan, P. Senguttuvan, V. G. Pol and S. K. Martha, Synergistic Mn-Cr Co-doping in $Na_3V_2(PO_4)_2O_2F$ Promising Cathode: Unlocking Superior Performance for Next-Generation Sodium-Ion Batteries, *Small*, 2025, **21**, 2504006.
33. Q. Wu, Y. Z. Ma, S. Q. Zhang, X. Chen, J. B. Bai, H. Wang and X. J. Liu, Achieving a Rapid Na+ Migration and Highly Reversible Phase Transition of NASICON for Sodium-Ion Batteries with Suppressed Voltage Hysteresis and Ultralong Lifespan, *Small*, 2024, **20**, 2404660.
34. G. S. Su, Y. J. Wang, J. W. Mu, Y. F. Ren, P. Yue, W. X. Ji, L. W. Liang, L. R. Hou, M. Chen and C. Z. Yuan, Insights into Tiny High-Entropy Doping Promising Efficient Sodium Storage of $Na_3V_2(PO_4)_2O_2F$ toward Sodium-Ion Batteries, *Adv. Energy Mater.*, 2025, **15**, 2403282.
35. Q. X. Hu, M. J. Sun, Y. C. Zha, G. Q. Zhao, H. L. Tang, L. Yang, M. Yang, B. H. Pang, Y. J. Sun and H. Guo, Ti Substitution Strategy Improves Electrochemical Performance of $Na_3V_2(PO_4)_2F_3$ Cathode, *ACS Energy Lett.*, 2025, **10**, 1840-1850.
36. H. Yu, H. B. Jing, Y. Gao, X. M. Wang, Z. Y. Gu, L. S. Li, J. J. Wang, S. Y. Wang, X. L. Wu, W. H. Qi, Q. H. Liang and C. F. Du, Unlocking the Sodium Storage Potential in Fluorophosphate Cathodes: Electrostatic Interaction Lowering Versus Structural Disordering, *Adv. Mater.*, 2025, **37**, 2400229.